Temporal variation of the photometric magnetic activity for the Sun and *Kepler* solar-like stars

A. R. G. Santos[1,2], S. Mathur[3,4], R. A. García[5], A.-M. Broomhall[2], R. Egeland[6], A. Jiménez[3,4], D. Godoy-Rivera[3,4], S. N. Breton[7,8], Z. R. Claytor[9,10], T. S. Metcalfe[11], M. S. Cunha[1], and L. Amard[5]

[1] Instituto de Astrofísica e Ciências do Espaço, Universidade do Porto, CAUP, Rua das Estrelas, PT4150-762 Porto, Portugal
   e-mail: Angela.Santos@astro.up.pt
[2] Department of Physics, University of Warwick, Coventry, CV4 7AL, UK
[3] Instituto de Astrofísica de Canarias (IAC), E-38205 La Laguna, Tenerife, Spain
[4] Universidad de La Laguna (ULL), Departamento de Astrofísica, E-38206 La Laguna, Tenerife, Spain
[5] Université Paris-Saclay, Université Paris Cité, CEA, CNRS, AIM, 91191, Gif-sur-Yvette, France
[6] High Altitude Observatory, National Center for Atmospheric Research, P.O. Box 3000, Boulder, CO 80307-3000, USA
[7] Université Paris Cité, Université Paris-Saclay, CEA, CNRS, AIM, 91191, Gif-sur-Yvette, France
[8] INAF – Osservatorio Astrofisico di Catania, Via S. Sofia, 78, 95123 Catania, Italy
[9] Department of Astronomy, University of Florida, 211 Bryant Space Science Center, Gainesville, FL 32611, USA
[10] Institute for Astronomy, University of Hawai'i at Mānoa, 2680 Woodlawn Drive, Honolulu, Hawai'i 96822, USA
[11] White Dwarf Research Corporation, 9020 Brumm Trail, Golden, CO 80403, USA

April 7, 2023

ABSTRACT

Context. The photometric time series of solar-like stars can exhibit rotational modulation, that is, brightness variations due to active regions co-rotating with the stellar surface. These signatures allow us to constrain properties of stellar rotation and magnetic activity.
Aims. In this work we investigate the behavior, particularly the variability in terms of strength, of the photometric magnetic activity of *Kepler* solar-like stars and compare it with that of the Sun.
Methods. We adopted the photometric magnetic activity proxy, S_{ph}, which was computed with a cadence of five times the rotation period (P_{rot}). The average S_{ph} was taken as the mean activity level, and the standard deviation was taken as a measure of the temporal variation of the magnetic activity over the *Kepler* observations. We also analyzed Sun-as-a-star photometric data from VIRGO (Variability of Solar Irradiance and Gravity Oscillations). Sun-like stars were selected from a very narrow parameter space around the solar properties, according to the recent *Gaia-Kepler* stellar properties catalog and the latest *Kepler* rotation catalog. We also looked into KIC 8006161 (HD 173701), a very active metal-rich G dwarf, and we compared its magnetic activity to that of stars with similar stellar fundamental parameters.
Results. We find that the amplitude of S_{ph} variability is strongly correlated with its mean value, independent of spectral type. An equivalent relationship has previously been found for ground-based observations of chromospheric activity emission and magnetic field strength, but in this work we show that photometric *Kepler* data also present the same behavior. While, depending on the phase of the cycle, the Sun is among the less active stars, we find that the $S_{ph\odot}$ properties are consistent with those observed in *Kepler* Sun-like stars. KIC 8006161 is, however, among the most active of its peers, which tend to be metal-rich. This results from an underlying relationship between P_{rot} and metallicity and supports the following interpretation of the magnetic activity of KIC 8006161: its strong activity is a consequence of its high metallicity, which affects the depth of the convection zone and, consequently, the efficiency of the dynamo.

Key words. stars: low-mass – stars: rotation – stars: activity – starspots – stars: individual: HD 173701 – Sun: activity – techniques: photometric – methods: data analysis

1. Introduction

Low-mass stars with convective envelopes, particularly stars of spectral type FGKM (hereafter solar-like stars), can be magnetically active (e.g., Brun & Browning 2017). As with the Sun, the emergence of dark magnetic spots at the surface is one of the manifestations of their magnetic activity. As stars rotate, the dark starspots go in and out of view while modulating the stellar brightness. Bright faculae in active regions can also produce rotational modulation; however, their intensity contrast is smaller. Hence, the rotational modulation contains information on stellar surface rotation and magnetic activity. Both of these properties are strongly dependent on stellar age (e.g., Wilson 1963; Wilson & Skumanich 1964; Skumanich 1972; Kawaler 1988). In particular, during their main sequence, as stars evolve and lose angular momentum due to magnetic braking, they spin down following the so-called Skumanich law (Skumanich 1972). The possibility of constraining stellar ages through surface rotation measurements led to the formulation of gyrochronology (Barnes 2003), which is also mass dependent. After solar-like stars converge to a narrow rotation sequence, lower-mass stars spin down faster than higher-mass stars (e.g., Barnes 2003, 2007; van Saders & Pinsonneault 2013; Matt et al. 2015). However, stars above the Kraft break ($T_{eff} > 6250$ K; Kraft 1967), with very shallow convective envelopes, are unable to spin down significantly.

Space-based photometric planet-hunting missions provide a unique opportunity to characterize stars. Namely, the *Kepler* main mission (Borucki et al. 2010) obtained unmatched long-term and continuous observations for hundreds of thousands of stars (e.g., Mathur et al. 2017). For those exhibiting rotational modulation (i.e., several tens of thousands of solar-like stars), *Kepler* data allowed average surface rotation periods ($P_{\rm rot}$) to be measured (e.g., Nielsen et al. 2013; Reinhold et al. 2013; McQuillan et al. 2013, 2014; García et al. 2014a; Ceillier et al. 2016, 2017; Santos et al. 2019b, 2021a; Breton et al. 2021). For main-sequence *Kepler* solar-like stars, surface rotation periods generally decrease with increasing effective temperature: M stars have a median period of ~ 40 days, while for F stars the median period is ~ 10 days. This general dependence is consistent with the expected rotation evolution (e.g., Barnes 2003; van Saders & Pinsonneault 2013; Matt et al. 2015) and also with the narrow rotation sequences in cluster data (e.g., Barnes 2003; Agüeros et al. 2011; Rebull et al. 2016; Fritzewski et al. 2021; Boyle & Bouma 2022). Interestingly, for *Kepler* GKM main-sequence (i.e., dwarfs) stars, which span a relatively wide range of ages, the rotation-period distribution is bimodal and stars tend to group into two populations or groups. The two populations are separated by an intermediate-$P_{\rm rot}$ gap.

When first discovered, the bimodal rotation-period distribution was thought to be a feature of the *Kepler* field, and its origin was attributed to two distinct epochs of star formation (McQuillan et al. 2013, 2014, see also Davenport & Covey 2018). However, it is now known that the rotation-period distribution is also bimodal across the different fields of view of the extended *Kepler* mission, K2 (Howell et al. 2014), as reported by Reinhold & Hekker (2020) and Gordon et al. (2021). Two other hypotheses have been suggested to explain this phenomenon. Montet et al. (2017) and Reinhold et al. (2019) find evidence for the stars in the fast-rotating population being spot-dominated and those in the slow-rotating population being faculae-dominated. In this context, stars would transition from spot- to faculae-dominated and the "gap" in the rotation distribution would be an artifact resulting from a lack of rotation detections due to the cancelation between the dark spots and the bright faculae (Reinhold et al. 2019). Another interpretation of the bimodal rotation distribution has also been proposed: a broken spin-down law (McQuillan et al. 2014; Angus et al. 2020; Spada & Lanzafame 2020; Gordon et al. 2021; Lu et al. 2022). While decoupled from the core, the surface of stars on the fast-rotating population spins down due to magnetic braking, following the Skumanich law. As the fast-rotating core and the envelope start to couple, the surface spin-down would cease. This transition would be relatively fast, leading to the intermediate-$P_{\rm rot}$ gap. Having completed the coupling (reaching the slow-rotating population), the stellar surface would start to spin down again following the Skumanich law. Recently, evidence supporting this interpretation of the intermediate-$P_{\rm rot}$ gap was found in ground-based photometric data by Lu et al. (2022). The authors find that the gap is absent in the regime of fully convective stars, while it is still found for the partially convective stars.

In addition to surface rotation, spot modulation also allows stellar magnetic activity to be constrained. Despite the degeneracy between different parameters, the amplitude of the rotational signal in the light curve is related to the spot coverage of the stellar surface, which in turn is related to the magnetic activity level of the star. Based on this and developing upon the starspot proxy used in García et al. (2010), Mathur et al. (2014) defined the photometric magnetic activity index, $S_{\rm ph}$. It is a measurement of the amplitude of the rotational modulation and has been shown to be an adequate proxy of solar and stellar magnetic activity (Salabert et al. 2016a, 2017). For the Sun, Salabert et al. (2017) demonstrated that the $S_{\rm ph}$ is well correlated with other, more conventional, proxies of magnetic activity, such as the sunspot number, sunspot areas (SAs), Ca H-K emission, and radio flux. Based on seismic solar analogs observed by *Kepler*, $S_{\rm ph}$ was also found to be complementary to the Ca H-K emission for stars other than the Sun (Salabert et al. 2016a; Karoff et al. 2018, see also Egeland et al. in prep.). For *Kepler* main-sequence solar-like stars, the dependence of $S_{\rm ph}$ on effective temperature is complex (Santos et al. 2019b, 2021a). M stars tend to have large $S_{\rm ph}$; the $S_{\rm ph}$ slightly decreases toward late-type K stars. From ~ 4000 K to ~ 6000 K, the range of $S_{\rm ph}$ widens: the upper edge of the $S_{\rm ph}$ distribution moves toward larger $S_{\rm ph}$ values, while the lower edge moves toward smaller values and changes more drastically. F stars typically have small $S_{\rm ph}$, which may be attributed to their shallow convective envelopes and to their fast evolution, which also may contribute to short activity lifetimes (e.g., Reiners & Mohanty 2012).

Generally, fast-rotating stars are expected to have a stronger magnetic activity in comparison with slow-rotating stars as a result of the efficiency of the dynamo. Indeed, such a relationship has been observed in chromospheric and coronal magnetic activity proxies (APs; e.g., Vaughan et al. 1981; Baliunas et al. 1983; Noyes et al. 1984; Soderblom et al. 1993; Wright et al. 2011). Similarly, for the *Kepler* solar-like stars, the average photometric AP, $S_{\rm ph}$, tends to increase with decreasing rotation period (Santos et al. 2019b, 2021a). However, the activity-rotation relationship is not linear. In fact, because of the $P_{\rm rot}$ bimodality and intermediate-$P_{\rm rot}$ gap in the *Kepler* field mentioned above, the $S_{\rm ph}$ versus $P_{\rm rot}$ diagram exhibits two different regimes: for instance, for K stars there are two almost parallel populations. While the $P_{\rm rot}$ distribution of F stars is not bimodal, there are also two groups of stars with different behaviors: those below the Kraft break and those above (see Appendix B in Santos et al. 2021a). For late F stars below the Kraft break ($T_{\rm eff} < 6250$ K), $P_{\rm rot}$ and $S_{\rm ph}$ are well correlated, similar to what is found for cooler solar-like stars. For stars above the Kraft break ($T_{\rm eff} > 6250$ K), the correlation between $P_{\rm rot}$ and $S_{\rm ph}$ is very weak, and a group of low-activity fast rotators emerges. As mentioned above, their thin convective envelopes may not be able to harbor a strong surface magnetic activity; therefore, these stars do not brake significantly along the main sequence either. Furthermore, the *Kepler* F-star sample includes stars of different absolute and relative ages, and evolved F stars have been found to be among the most inactive stars in other stellar samples (e.g., Wright 2004; Schröder et al. 2013).

In addition to the intermediate-$P_{\rm rot}$ gap and the Kraft break, other transitions in the activity-rotation relationship have been reported for solar-like stars. Particularly, at activity levels consistent with the slow-rotating population, that is, stars with longer $P_{\rm rot}$ than the intermediate-$P_{\rm rot}$ gap, there is a lack of stars with intermediate Ca H-K emission, which is known as the Vaughan-Preston (VP) gap (e.g., Vaughan & Preston 1980; Vaughan 1980; Henry et al. 1996; Gomes da Silva et al. 2021). However, so far, such a gap has not been found in the photometric magnetic activity of *Kepler* stars.

In this work we investigate the temporal variability of the photometric magnetic AP, $S_{\rm ph}$, over the *Kepler* observations and compare the $S_{\rm ph}$ behavior with the photometric magnetic activity of the Sun. The paper is organized as follows. We summarize the data and the target sample of this work in Sect. 2. Section 3 briefly describes the adopted magnetic AP, $S_{\rm ph}$. In Sect. 4 we show our results for the Sun and solar-like stars. Moreover, by

selecting stars very similar to the Sun and to KIC 8006161, a metal-rich solar analog with a known magnetic activity cycle, we investigate how the behavior of these stars matches that of the others. Section 5 presents a further discussion and our conclusions.

2. Data preparation and sample selection

2.1. Data preparation

In this work, we analyze the KEPSEISMIC[1] data products obtained from *Kepler* long-cadence data ($\Delta t = 29.42$ min; Borucki et al. 2010) with the *Kepler* Asteroseismic Data Analysis and Calibration Software (KADACS; García et al. 2011). KEPSEISMIC data were optimized for seismic studies and are also proper for the analysis of spot modulation in the light curves (Santos et al. 2019b, 2021a). KEPSEISMIC data are obtained with customized apertures and corrected for outliers, jumps, drifts, and discontinuities at the *Kepler* Quarter edges. In addition, gaps smaller than 20 days were filled using in-painting techniques (see García et al. 2014b; Pires et al. 2015). Finally, the light curves were high-pass filtered at 20, 55, and 80 days (i.e., three KEPSEISMIC light curves were analyzed per star). While the filters with short cutoff period are more efficient at minimizing the *Kepler* instrumental effects, they can also filter the long-period stellar signal. Therefore, Santos et al. (2019b, 2021a) conducted a parallel analysis of the different filtered light curves in order to find the best compromise between filtering out the instrumental modulations and preserving the rotational signal. Filtering the instrumental modulation is also useful to reduce the bias on the photometric magnetic AP, $S_{\rm ph}$. The choice for the most adequate filter for each target was already made in Santos et al. (2019b, 2021a). We note that periods longer than the cut-off period of a given filter employed by KADACS can still be retrieved, as the filter transfer function slowly reaches zero at twice the cut-off period.

Average rotation period and average $S_{\rm ph}$ are adopted from Santos et al. (2019b, 2021a). The rotation pipeline used by the authors employs three rotation diagnostics: wavelet analysis, autocorrelation function (ACF), and composite spectrum (CS; e.g., Mathur et al. 2010; García et al. 2014a; Ceillier et al. 2016, 2017). The latter diagnostic combines the former two, highlighting the common peaks and attenuating the remainder, which is particularly relevant to avoid false positives due to, for example, instrumental effects or high-amplitude second and third harmonics. For each target there are nine period estimates (three per light curve). The final rotation periods were selected in three steps: automatic selection, which requires agreement between different estimates and a minimum height of the corresponding rotation peaks; machine learning through the implementation of ROOSTER (Random fOrest Over STEllar Rotation; Breton et al. 2021), which, after an adequate training, was fed with stellar parameters, the output parameters from the rotation pipeline, and the associated $S_{\rm ph}$ values; and complementary visual inspection. In all steps, the priority was given to the period-estimate from the wavelet analysis, which allows for a conservative approach, providing associated uncertainties of about 10% in average. Further details are available in Santos et al. (2019b, 2021a) and Breton et al. (2021).

For the stellar effective temperature ($T_{\rm eff}$), surface gravity (log g), and metallicity ([Fe/H]), we prioritized spectroscopic constraints when available; otherwise, we resorted to photometric values. The order of prioritization is as follows: *Kepler* Community Follow-up Observation Program (CFOP) in high resolution (Furlan et al. 2018); Apache Point Observatory for Galactic Evolution Experiment (APOGEE; Ahumada et al. 2020); Large Sky Area Multi-Object Fiber Spectroscopic Telescope (LAMOST; Zhao et al. 2012; Zong et al. 2020); the *Gaia-Kepler* Stellar Properties Catalog (GKSPC; Berger et al. 2020); and *Kepler* Stellar Properties Catalog for Data Release 25 (KSPC DR25; Mathur et al. 2017). We also adopted the model luminosities (L) and equivalent evolutionary phases (EEPs) obtained in Mathur et al. (in prep.) using the implementation of the Yale Rotation Evolution Code by van Saders & Pinsonneault (2013) and van Saders et al. (2016) and the interpolation tool by Claytor et al. (2020a,b, `kiauhoku`). Finally, in Appendix B we also adopt the renormalized unit-weight error (RUWE; Gaia Collaboration et al. 2016, 2021; Lindegren et al. 2021).

To place the Sun in context of solar-like stars, we used more than 24 years of data from the Variability of Solar Irradiance and Gravity Oscillations (VIRGO) sun photometer (SPM), which is on board the Solar and Heliospheric Observatory (SoHO; Domingo et al. 1995; Fröhlich et al. 1995, 1997; Jiménez et al. 2002), covering two full solar cycles: starting on 23 January 1996 and ending on 15 May 2021. For the final solar light curve, we only combined the GREEN and RED channels (hereafter VIRGO g+r), which best represent the *Kepler* bandwidth (Basri et al. 2010). VIRGO/SPM collects observations with a cadence of 60 seconds, and thus we re-binned the data to 30 minutes to be consistent with *Kepler* long-cadence data and reduce computing time (note that a long cadence is sufficient to study the rotational modulation of *Kepler* solar-like stars, whose characteristic timescales are relatively long).

In Appendix A we also use the daily records for the SAs[2] and for the solar flux at 10.7 cm[3] ($F_{10.7}$). Sunspot areas are expressed in millionths of a solar hemisphere (μHem), while $F_{10.7}$ is expressed in solar flux units (sfu; i.e., $10^{22}\,{\rm W\,m^{-2}\,Hz^{-1}}$). The SA and $F_{10.7}$ records are available since 1 May 1874 and 17 February 1947, respectively. Sunspot areas, which correspond to the total sunspot coverage of the solar disk, are directly linked to the strong component of the magnetic field in the photosphere. $F_{10.7}$ is sensitive to both strong and weak components of the solar magnetic field in the upper chromosphere and lower corona (e.g., Covington 1969; Tapping 1987; Tapping & Detracey 1990).

2.2. Sample selection

We started with the 55,232 stars of spectral type mid-F to M from Santos et al. (2019b, 2021a). Potential contaminants, such as eclipsing binaries, misclassified red giants, and classical pulsators, were discarded by the authors for the rotational analysis.

To further avoid biases, in this work, we also neglected the targets that required particular care to retrieve the correct rotation period due to the presence of high-amplitude instrumental modulation. Those were identified and corrected during the visual inspection in Santos et al. (2019b, 2021a). We also removed the targets for which we had to consider an individual photon-shot-noise correction (see Sect. 3 and Santos et al. 2019b, 2021a) to ensure that the $S_{\rm ph}$ values are computed in a homogeneous way. These two criteria removed 2,758 targets.

We also removed from the sample targets that have been identified as potential binaries: *Gaia* DR2 and DR3 binaries (Berger et al. 2018; Gaia Collaboration et al. 2022, 2,305 tar-

---

[1] MAST: https://doi.org/10.17909/t9-mrpw-gc07

[2] solarcyclescience.com
[3] www.ngdc.noaa.gov

gets), tidally synchronized binaries (Simonian et al. 2019, 130 targets), and close-in binary candidates (Santos et al. 2019b, 2021a, 2,486). The respective flags were provided in Santos et al. (2019b, 2021a). The quasi-periodic modulation seen in close-in binary candidates identified by Santos et al. (2019b, 2021a) can still be related to rotation. However, there are some striking differences between their signal and the typical rotation signature of solar-like stars. Close-in binary candidates have very large average S_{ph} values, fast and stable beating patterns, and a long chain of high-amplitude harmonics. As shown in Santos et al. (2019b, 2021a), the close-in binary candidates tend to have shorter periods than the lower edge (5th percentile) of the P_{rot} distribution at a given effective temperature and tend to be beyond the upper edge (95th percentile) of the $\langle S_{ph} \rangle$ distribution. Interestingly, these targets and those classified as tidally synchronized binaries by Simonian et al. (2019) occupy the same parameter space in terms of average P_{rot} and S_{ph}, tending to be outliers in comparison with solar-like stars of similar effective temperature.

Targets fainter than *Kepler* magnitude Kp = 16 were also neglected (1,774 targets), as their light curves tend to be noisier than those of bright stars. Furthermore, to ensure that one has a more complete picture of the stellar magnetic activity, we removed light curves with a time span shorter than 12 *Kepler* Quarters (3,179 targets).

Removing the targets described above[4], the final target sample for the current study comprises 44,605 targets: 41,931 main-sequence stars (426 M; 13,499 K; 20,235 G; and 7,771 F) and 2,674 subgiant stars. The evolutionary stage of the targets is determined through the EEPs from Mathur et al. (in prep.). The T_{eff} cuts adopted to split the sample into spectral types FGKM are 6000 K, 5200 K, and 3700 K, respectively. For the final sample, we have CFOP parameters for 361 targets, APOGEE parameters for 2,026 targets, LAMOST parameters for 14,493 targets, GKSPC parameters for 26,183 targets, and KSPC DR25 parameters 1,542 targets. The Hertzsprung–Russell (HR) diagram for the target sample is shown in Appendix B.2.

Appendix B provides more details about the targets that were neglected in the context of the parameters we study below. While removing targets that seem to behave normally, the selection criteria above also remove a significant amount of outliers. Despite the attempt to remove all binary candidates as described above, there is a concern related to additional potential binaries. For this reason, in Appendixes B and C, we also considered the RUWE values, but we do not find any particular bias in terms of rotation or photometric magnetic activity.

3. Photometric magnetic activity proxy

The photometric magnetic AP, S_{ph}, is the standard deviation of light curve segments of length $5 \times P_{rot}$ as defined by Mathur et al. (2014). Salabert et al. (2016a, 2017) show that S_{ph} is a proper proxy for solar and stellar magnetic activity. However, we note that S_{ph} can be a lower limit of the maximum possible photometric activity level. The S_{ph} values depend on the spot visibility, which is determined by the stellar inclination angle and the spot latitudinal distribution. Furthermore, the longitudinal distribution of spots also affects S_{ph}; for example S_{ph} is relatively small when spots are on opposite sides of the star. This potential underestimation of the photometric magnetic activity may be important for individual targets, particularly with small incli-

---

[4] The numbers of targets listed at each cut are not exclusive, as a given target may not obey multiple selection criteria (e.g., the same target may be both faint and flagged as binary candidate).

nation angles, but its effect should not be significant in ensemble studies.

As mentioned above, the average S_{ph} values, $\langle S_{ph} \rangle$, were adopted from Santos et al. (2019b, 2021a) for the *Kepler* solar-like stars. These were corrected for the photon-shot noise following the approach by Jenkins et al. (2010). For the VIRGO/SPM data, the correction to the photon-shot noise was computed from the high-frequency (8000-8200 μHz) noise in the power spectrum density (PSD) for the original 60-second cadence. This estimate computed from the PSD is an upper limit to the photon-shot noise in the solar observations.

In addition to the average S_{ph}, in this study we also computed the temporal variation of S_{ph} by computing the standard deviation of the individual S_{ph} values computed over $5 \times P_{rot}$ segments. Given that S_{ph} is a proxy for magnetic activity, a time series of S_{ph} over the 4 yr *Kepler* mission provides a brief window into the long-term, cycle-scale variability of the star, as we demonstrate using the Sun in the following section. The standard deviation of S_{ph} therefore provides a lower-limit estimate of the amplitude of long-term variability for our sample of stars.

4. Results

4.1. Photometric magnetic activity of the Sun

For consistency with the *Kepler* bandpass, we analyzed Sun-as-a-star VIRGO g+r photometric data (Basri et al. 2010). To compute the S_{ph} over segments of length $5 \times P_{rot}$, we used $P_{rot\odot} = 26.43 \pm 1.04$ days. The rotational analysis and the individual S_{ph} values for solar cycles 23 and 24 are shown in Appendix A.

Next, we split the S_{ph} data into segments of 4 years, which is the maximum length of the *Kepler* observations. The segments are spaced by 1 year in order to cover a wide range of phases of the activity cycle. We also consider one last segment with a length of about 3 years, which is the minimum observational length considered in this work (Sect. 2.2). In total, we have 22 S_{ph} segments. For each segment we computed the average and the standard deviation of the individual S_{ph} values (shown in Fig. 1).
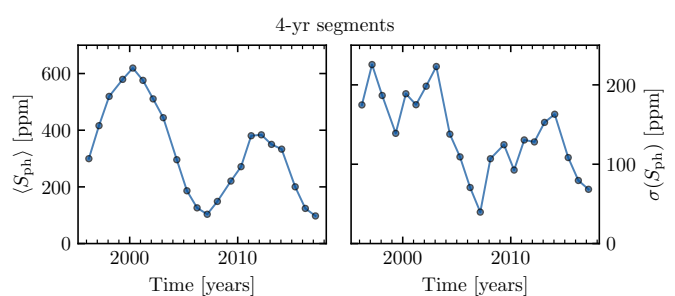

Fig. 1. Average (left) and the standard deviation (right) of the individual S_{ph} values over 4 yr segments for VIRGO g+r. The horizontal axis corresponds to the starting time of the 4 yr segment.

The average S_{ph} follows the 11 yr magnetic activity cycle of the Sun, while the $\sigma(S_{ph})$ tends to be largest at high activity levels, but is not exactly in phase with $\langle S_{ph} \rangle$. In fact, one can see the signature of the so-called quasi-biennial oscillations (QBOs) in the 4-year $\sigma(S_{ph})$ around the activity maxima (see also SA and $F_{10.7}$ behavior in Appendix A). Quasi-biennial oscillations are quasi-periodic short-term variations in the solar magnetic activity and are seen in different magnetic APs of the Sun (e.g.,

Broomhall et al. 2012; Bazilevskaya et al. 2014; Broomhall & Nakariakov 2015; Mehta et al. 2022). They are present at all phases of the 11 yr solar cycle, being modulated by it. However, because we are using 4 yr segments, in Fig. 1, the QBO signature is only found around the maxima, where the QBO amplitude is the largest.

4.2. Photometric magnetic activity of the solar-like stars

In this work, we investigate the relation between the average photometric magnetic activity, $\langle S_{ph} \rangle$, and its variation, $\sigma(S_{ph})$, over the *Kepler* observations of tens of thousands of solar-like stars with detectable rotational modulation. Furthermore, we compare their S_{ph} behavior with that of the Sun.

Figure 2 shows the $\sigma(S_{ph})$ versus $\langle S_{ph} \rangle$ relation for the main-sequence stars of different spectral types and also for the sub-giant stars. We find a tight relation between $\sigma(S_{ph})$ and $\langle S_{ph} \rangle$, with $\sigma(S_{ph})$ increasing with $\langle S_{ph} \rangle$. This suggests that stars that are on average photometrically more active are also more variable in time. Indeed, given that S_{ph} has been shown to be a valid magnetic AP, this result is not surprising and it is consistent with the results from ground-based spectroscopic observations, where different authors found that stars with large chromospheric emissions also exhibit large temporal variations (e.g., Wilson 1978; Radick et al. 1998, 2018; Lockwood et al. 2007; Egeland 2017; Gomes da Silva et al. 2021; Brown et al. 2022). Furthermore, Brown et al. (2022) showed that the surface-averaged magnetic field strength also exhibits a similar behavior, with its temporal variation being the largest for stars with the strongest average magnetic field.

The results for the Sun are overplotted in blue in the different panels of Fig. 2. The blue star marks the standard deviation and average solar S_{ph} values measured from full VIRGO g+r light curve ($\sim$ 24 yr). The blue circles correspond to the $\langle S_{ph} \rangle$ and $\sigma(S_{ph})$ measured from 4-year segments, representing different phases of the cycle (Sect. 4.1). While the 4-year $\langle S_{ph} \rangle$ and $\sigma(S_{ph})$ for the Sun span a wide range of values, they tend to follow the general relation seen for the *Kepler* solar-like stars, with phases of high activity level having greater variations in comparison with the low activity phases. However, there is some deviation from the general trend, for example around the solar maximum (see Fig. 1), where the signature of the QBO is present (Sect. 4.1). This translates into a larger scatter in Fig. 2 around larger values of solar $\langle S_{ph} \rangle$, shown in blue.

KIC 8006161 (HD 173701) is also highlighted in Fig. 2 in turquoise. KIC 8006161, popularly known as Doris, is a seismic solar analog with a confirmed $\sim$ 8 yr magnetic activity cycle. KIC 8006161, with a surface P_{rot} of about 30 days, is rotating more slowly than the Sun, but it is reported to be significantly more active (Karoff et al. 2018). In addition of being a well characterized G dwarf, its activity cycle was confirmed with independent spectroscopic ground-based observations (Karoff et al. 2018) spanning almost 20 years and also being partially contemporaneous to the *Kepler* observations. The activity cycle is also detected in different APs, including asteroseismic ones. These attributes make KIC 8006161 a reference *Kepler* solar-like star. KIC 8006161 is also intriguing and often seen as an outlier, which may be related to its high metallicity ([Fe/H] = 0.34; Furlan et al. 2018) and enhanced magnetic activity. Details on the properties of KIC 8006161 are available in Karoff et al. (2018) and references therein. *Kepler* observed part of the rising phase of one cycle, starting around the activity minimum (e.g., Kiefer et al. 2017; Karoff et al. 2018; Santos et al. 2018). The minimum and maximum S_{ph} values are $\sim$ 396 and $\sim$ 1262 ppm,
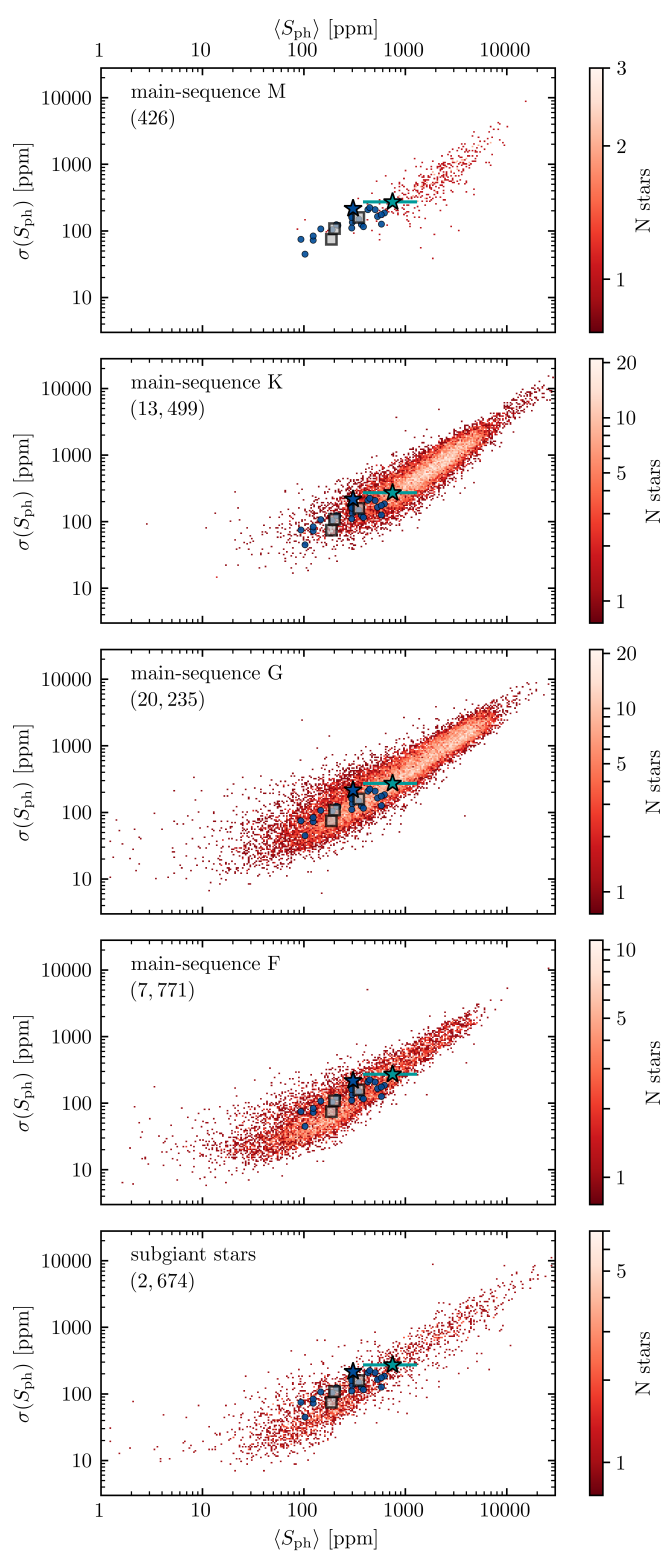

Fig. 2. Standard deviation of S_{ph} as a function of the average S_{ph} for main-sequence stars of different spectral types and subgiants, color-coded by the number of stars. The blue star marks the solar values from the 24 yr VIRGO g+r, while the blue circles indicate the values obtained from 4 yr segments. The turquoise star highlights Doris (KIC 8006161), a solar analog with a confirmed 8 yr activity cycle. The turquoise line indicates the range between minimum and maximum individual S_{ph} values. The squares mark three activity-cycle candidates: KIC 5184732, KIC 7970740, and KIC 10644253. The number of *Kepler* targets of each type is indicated in each panel.

respectively. The turquoise line marks the range between these values, while the turquoise star indicates the average and standard deviation of the individual S_{ph} over the 4 yr *Kepler* observations. We also highlight three other stars (squares) that show evidence for cyclic magnetic activity both seen through S_{ph} and asteroseismic indicators (e.g., Salabert et al. 2016b; Santos et al. 2018). However, these potential magnetic cycles are not independently confirmed, and thus they should be still considered as candidates. From less to more photometrically active, the three stars are: KIC 5184732 (G dwarf), KIC 7970740 (G dwarf), and KIC 10644253 (F dwarf, a young seismic solar analog). Similarly to the Sun, KIC 8006161 and the other highlighted stars follow the observed $\sigma(S_{ph})$ versus $\langle S_{ph} \rangle$ relation. All four *Kepler* stars are part of the asteroseismic LEGACY sample (Lund et al. 2017; Silva Aguirre et al. 2017).

In the $\sigma(S_{ph})$ versus $\langle S_{ph} \rangle$ relation shown in Fig. 2, there are underlying dependences on other stellar properties. For example, $\langle S_{ph} \rangle$ depends on P_{rot} and T_{eff} (e.g., Santos et al. 2019b, 2021a) and it may also depend on L, which changes as stars evolve and become less active. Thus, to make sure that we account for all potential bias, we perform a multivariate linear regression to account for dependences on different parameters: *Kepler* magnitude (Kp), observational length (t_{obs}), effective temperature (T_{eff}), luminosity (L), metallicity [Fe/H], P_{rot}, and $\langle S_{ph} \rangle$. Here we consider the logarithm of the $\sigma(S_{ph})$ and $\langle S_{ph} \rangle$. Table 1 lists the Spearman correlation coefficients (SCCs), which were computed between a given property and the residuals after isolating the dependence on that property (i.e., removing the dependences on the remainder). We only find significant and systematic correlations with P_{rot} and $\log \langle S_{ph} \rangle$. Appendix C summarizes the coefficients of the multivariate regression.

The SCC values are consistent with no or weak correlation between $\log \sigma(S_{ph})$ and t_{obs} or Kp. The positive SCC values for Kp indicate that $\sigma(S_{ph})$ increases toward faint stars, which typically have noisier light curves in comparison with bright stars. While there is a photon-shot noise correction applied to the S_{ph}, its variation can still be slightly affected by noise. The SCC values are negative for t_{obs}, indicating that shorter light curves have smaller $\sigma(S_{ph})$, which could be expected due to the smaller number of available data points. The SCC values for T_{eff}, L, and [Fe/H] are also consistent with no or weak correlation. Most of the atmospheric parameters are photometric (Sect. 2). Nevertheless, when considering solely the targets with spectroscopic constraints, we obtain similar results (Appendix C). The SCC values for P_{rot} are mostly consistent with moderate correlation, with the contrasting cases being the F dwarfs and the subgiants, which show very weak correlation between $\sigma(S_{ph})$ and P_{rot}. This correlation with P_{rot} is additional to the expected dependence in Fig. 2: $\langle S_{ph} \rangle$ generally increases with decreasing rotation period. The correlation between $\sigma(S_{ph})$ and P_{rot} can also be seen if we split the data into small ranges of S_{ph}: at roughly constant S_{ph}, slow rotators are less variable than fast rotators. Finally, as also suggested by Fig. 2, the correlation between $\log \sigma(S_{ph})$ and $\log \langle S_{ph} \rangle$ is very strong for all main-sequence spectral types and subgiants.

In Table 1, we also list the 5th and 95th percentiles of the $\langle S_{ph} \rangle$ distribution. The M dwarfs in the sample present large $\langle S_{ph} \rangle$ and, thus, large $\sigma(S_{ph})$, while F dwarfs tend to have smaller $\langle S_{ph} \rangle$ and $\sigma(S_{ph})$ in comparison with the cooler stars. The small $\langle S_{ph} \rangle$ values measured for F dwarfs (i.e., weak magnetic activity) may be a consequence of the shallower envelopes and less efficient dynamos unable to produce stellar winds to efficiently brake the stars. Therefore, F stars, specifically those above the Kraft break, remain fast rotators in the main sequence (e.g., van Saders & Pin-

sonneault 2013). Moreover, high-mass stars are also expected to have shorter activity lifetimes than the low-mass stars (Reiners & Mohanty 2012).

The results from the multivariate regression indicate that the relation between $\sigma(S_{ph})$ and $\langle S_{ph} \rangle$ becomes steeper as effective temperature decreases (from F to M). The slope values from the multivariate regression described above are listed in Appendix C and are shown by the blue circles in Fig 3. Trying to verify that there is no selection bias resulting from the different number of stars in each subsample, we conduct a resampling exercise. The smallest sample corresponds to the main-sequence stars of spectral type M (426 targets). Thus, we randomly select 426 stars from each remaining subsample (FGK dwarfs and subgiants) and we repeat the random selection 500 times. For each realization we perform a multivariate regression (as described above). The respective distributions of the slope for the $\log \sigma(S_{ph})$-$\log \langle S_{ph} \rangle$ relation are shown in light red in Fig. 3. The results retrieved from the resampling exercise are consistent with the general results, indicating that the relation is indeed steeper for the cooler stars in comparison with the hotter stars.
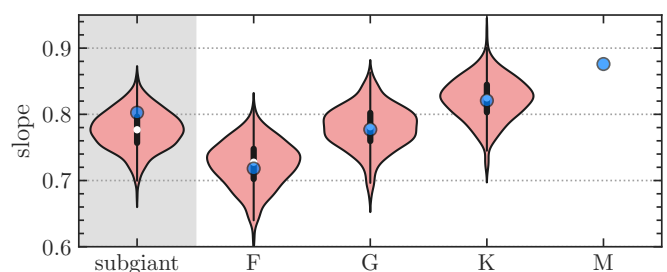

Fig. 3. Resampling results for the slope of the $\sigma(S_{ph})$ versus $\langle S_{ph} \rangle$ relation. The smallest subsample corresponds to the M dwarfs with only 426 targets. The resampling was done by randomly selecting 426 targets of the remaining subsamples and was repeated 500 times. For each realization, the multivariate linear regression was performed, and the final distributions for the slope are shown in light red. The thick black bars indicate the first and third quartiles, while the white circles indicate the second quartile. The blue circles indicate the values from the general multivariate regression performed with the full subsamples. The gray region marks the subgiant stars as their temperature does not follow the order of the main-sequence stars: for the dwarfs, T_{eff} increases from right to left.

4.2.1. P_{rot} bimodality: Fast- and slow-rotating populations

As described in the introduction, the rotation-period distribution for *Kepler* solar-like stars is bimodal (e.g., McQuillan et al. 2014; Santos et al. 2019b, 2021a). While the $\sigma(S_{ph})$ versus $\langle S_{ph} \rangle$ relation appears to be rather continuous, we pose the question of whether there is any substantial difference between the slow- and fast-rotating populations in terms of S_{ph} variation.

In the P_{rot}-T_{eff} diagram, the two regimes are separated by a lower density region, first noticed by McQuillan et al. (2014). The location of the period gap depends on the spectral type. In the activity-rotation diagram, one can also identify two regimes. While for the G dwarfs the fast-rotating regime seems almost saturated, it is clear for cooler stars that the fast-rotating regime is still rotation dependent. Comparably to what Reinhold & Hekker (2020) did for K2 stars, we split the two regimes by determining the local activity minimum between the populations in the activity-rotation diagram. The detailed procedure is described in Appendix B.3.

Figure 4 shows the $\sigma(S_{ph})$ versus $\langle S_{ph} \rangle$ relation for the fast- and slow-rotating populations for main-sequence GKM stars. The relation between the temporal variation of the photometric magnetic activity and its average values for the two populations does not seem to be distinct. For the K and G dwarfs, the stars in the fast-rotating population tend to have larger $\langle S_{ph} \rangle$ and, thus, larger $\sigma(S_{ph})$ in comparison with those in the slow-rotating population. Also, for all spectral types, the median luminosity is larger for the slow-rotating population than for the fast-rotating population, which generally is consistent with the slow rotators being more evolved than the fast rotators. Using the coefficients found for the multivariate regression for the full M-, K-, and G-dwarf samples, we correct each population for the dependences on the different observational and stellar properties. We find that the distributions of the $\log \sigma(S_{ph})$ residuals are similar and do not show a systematic trend. The most noticeable difference is that the relation (and distribution of the residuals) is tighter (narrower) for the fast-rotating population. We note, however, that the number of stars in the slow-rotating population is significantly larger than that of the fast-rotating population. We also perform a multivariate regression separately for each population, and there are no other clear systematic differences between the two populations. Table 1 and the tables in Appendix C summarize the properties of the $\sigma(S_{ph})$ versus $\langle S_{ph} \rangle$ relation and multivariate regression.

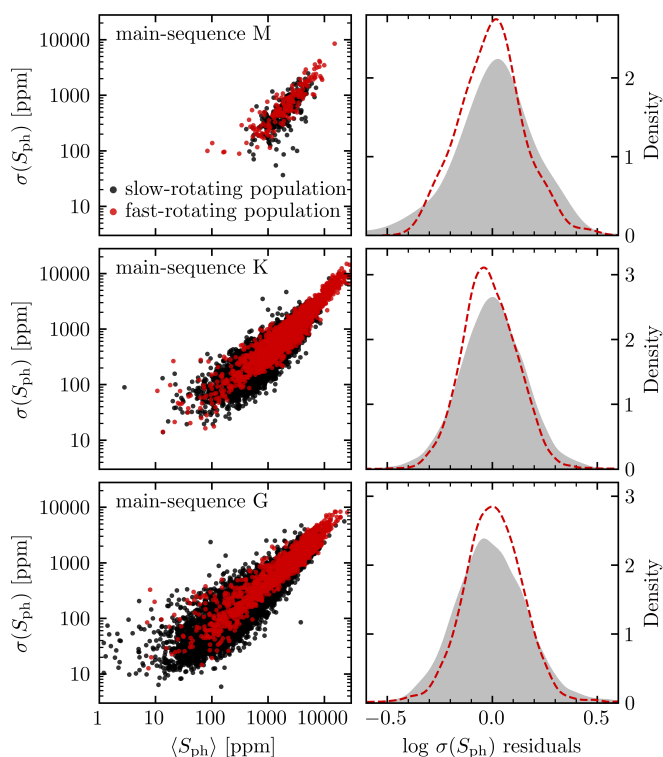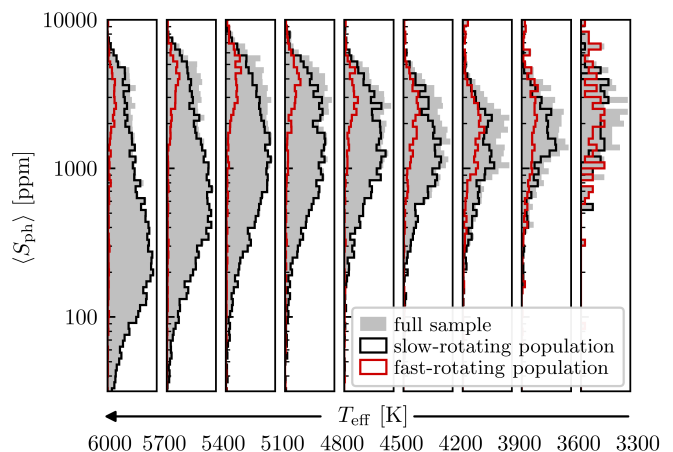## 4.2.2. Absence of the VP gap in Kepler photometric data

Fig. 5. $\langle S_{ph} \rangle$ distribution in logarithmic scale for the GKM dwarfs, split into T_{eff} intervals of 300 K. The gray shaded histogram shows the distribution for the full subsamples, while the solid black and red lines show the histograms for the slow- and fast-rotating populations, respectively. For clarity, the distributions here are shown by the actual histograms, while we opt for the KDE for the remainder.

In other stellar samples, there is a lack of stars with intermediate average chromospheric emission ($\log R'_{HK} \sim -4.75$; e.g., Vaughan & Preston 1980; Vaughan 1980; Henry et al. 1996; Gomes da Silva et al. 2021), which is known as VP gap. Gomes da Silva et al. (2021) and Brown et al. (2022) recently studied the average chromospheric emission and its variability for relatively large samples of stars (1,674 and 954 stars, respectively). While Gomes da Silva et al. (2021) found gaps in the data consistent with the VP gap, Brown et al. (2022) found under-density regions, which are less pronounced than the VP gap.

In the context of the *Kepler* sample, the VP gap would happen in the slow-rotating population. In Fig. 2, there is no evidence for gaps or discontinuities in the $\langle S_{ph} \rangle$ data for *Kepler* stars. Figure 5 shows the $\langle S_{ph} \rangle$ distribution for the GKM dwarfs in narrow T_{eff} intervals. The distributions for the slow- and fast-rotating populations are also plotted individually (solid-line histograms). In this figure, instead of using the kernel density estimate (KDE), we opt to show the histograms, so it is clear that the absence of gaps is not due to any kind of smoothing. We find that the $\langle S_{ph} \rangle$ distribution does not show clear gaps or lower density regions. Some of the bins for M dwarfs have lower density than the neighbor bins, but it might be due to the small number of M dwarfs (Table 1). The $\langle S_{ph} \rangle$ distributions for the fast- and slow-rotating populations are the least distinct for M dwarfs (see also the values corresponding to the 5th and 95th percentiles in Table 1). For K and G dwarfs, the distributions become more distinct, with the fast-rotating population having mostly large $\langle S_{ph} \rangle$ values. Nevertheless, while the distributions may not be exactly unimodal, this difference does not lead to a discontinuity in the distribution. Furthermore, we recall that the VP gap would be located in the slow-rotating population, not at the intermediate-P_{rot} gap. The distribution for the slow-rotating population also does not show evidence for discontinuity.

Fig. 4. Relation between $\sigma(S_{ph})$ and $\langle S_{ph} \rangle$ for the two populations of stars, above and below the intermediate-P_{rot} gap. *Left*: Same as in Fig. 2 but for main-sequence GKM stars. The color code indicates whether they belong to the fast- (red) or slow-rotating (black) populations. For F stars ($T_{eff} \geq 6000$ K), the rotation-period distribution is unimodal, and, thus, F stars are not considered here. *Right*: Distribution of the $\log \sigma(S_{ph})$ residuals computed after accounting for the dependences on the different parameters. The distributions for the fast- (red) or slow-rotating (gray) populations are illustrated by the KDE.

4.3. The Sun and the Sun-like stars

It has been a long-lasting question whether the Sun is a typical or unusual Sun-like star (e.g., Soderblom 1985; Lockwood et al. 1992; Henry et al. 1996; Gustafsson 1998; Egeland 2017). Recently, Reinhold et al. (2020) found that stars similar to the Sun observed by *Kepler* are notably more active than the Sun. This result was later questioned by Metcalfe & van Saders (2020), who showed that the stellar sample was biased toward lower T_{eff} and higher [Fe/H] in comparison to the Sun. In consequence, the selected stars might have deeper convection zones in comparison to the Sun, which in turn may be behind the strong magnetic activity measurements.

In this section we compare the Sun with the Sun-like stars, which are selected according to their effective temperature, surface gravity, and rotation period. Naturally, since the study by Reinhold et al. (2020), there were updates to these stellar properties. In Appendix B.4 for the Sun-like stars, we compare the updated parameters with those adopted by Reinhold et al. (2020) from Mathur et al. (2017). In this work, we adopted spectroscopic parameters when available (Zhao et al. 2012; Furlan et al. 2018; Zong et al. 2020; Ahumada et al. 2020). In practice, however, most of the adopted parameters turn out to be photometric ones from Berger et al. (2020), who took into account *Gaia* data and provided an update to the catalog by Mathur et al. (2017). Furthermore, rotation periods of *Kepler* solar-like (FGKM) stars have also been updated (Santos et al. 2019b, 2021a). Particularly, one of the most significant contributions in terms of new detections of rotational modulation and the respective period corresponds to targets close to the upper edge of the rotation distribution, where the Sun lies. Finally, the photometric magnetic activity metric used here and in Reinhold et al. (2020) are different. Differences between the two metrics are discussed for a sample of seismic targets with detected surface rotation in García et al. (2014a). Mathur et al. (in prep.) performs a detailed and extended comparison for the full sample of solar-like stars (not only seismic targets). The most significant discrepancies are at very low and very high activity levels.

As our G-dwarf subsample has a large number of targets, we can define a relatively narrow parameter space. The stars we selected as Sun-like stars have T_{eff} within 100 K, log L within 0.3 (in $L_\odot$), and P_{rot} within 2 days to those of the Sun. This selection results in 211 Sun-like stars. We considered the following solar values: $T_{eff\odot} = 5780$ K and $P_{rot\odot} = 26.43$ days. Figure 6 shows the HR diagram highlighting the Sun-like stars in shades of red, which indicate the metallicity of the stars. Below we discuss in detail and correct for the underlying dependences or biases.

Figure 7 shows the same as Fig. 2 but highlighting the Sun and the Sun-like stars (shades of red). The color code indicates the metallicity of the targets and those with spectroscopic constraints are marked by the black outline. The top and right-hand panels show the respective distributions for the Sun-like stars (red) and for the 4 yr solar segments (solid blue line). The blue dashed lines mark the values computed from the full 24 yr solar light curve. For this very narrow parameter space, $\langle S_{ph\odot} \rangle$ and $\sigma(S_{ph\odot})$ do not have a distinct behavior with respect to the Sun-like stars. However, for the Sun in the last two cycles, there are fewer epochs of large $\langle S_{ph\odot} \rangle$ compared to *Kepler* Sun-like stars. This difference is also seen in terms of the S_{ph} temporal variation.

Similarly to the previous sections, we corrected $\langle S_{ph} \rangle$ and $\sigma(S_{ph})$ for dependences on different properties. To compare with the Sun, we ignored Kp and t_{obs}, which, as verified above, show no significant correlations. The multivariate regressions are com-
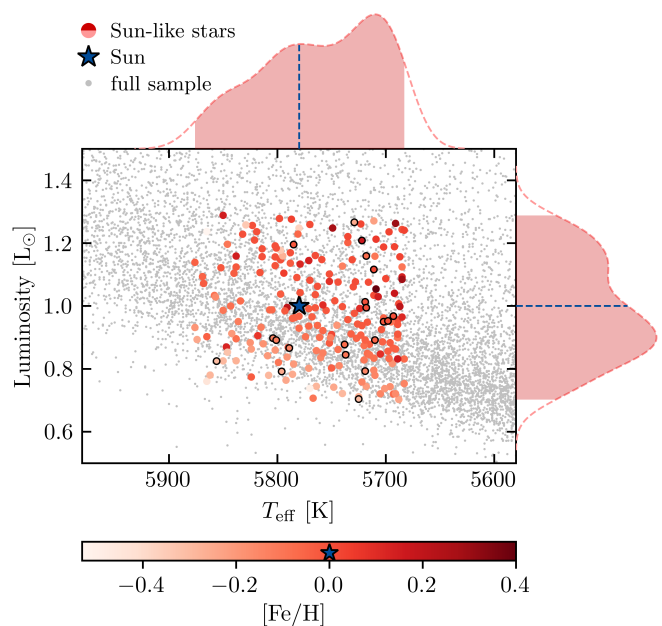

Fig. 6. HR diagram, where the 211 Sun-like stars (according to their T_{eff}, L, and P_{rot}) are highlighted in shades of red, which indicate the respective metallicity. The Sun is marked by the blue star. The top and right panels show the T_{eff} and L distributions, where the dashed blue lines mark the solar values. The symbols with a black outline mark the targets with spectroscopic constraints. As a reference, the gray dots show targets from the full target sample.

puted for the G stars shown in gray in Fig. 7. Then, we adopted the resulting coefficients to correct the $\langle S_{ph} \rangle$ and $\sigma(S_{ph})$ for the Sun-like stars and for the Sun. The results are summarized in Table 2 and in Appendix B.3).

As illustrated in Fig. 6, the sample of Sun-like stars is slightly biased toward low T_{eff} and low L in comparison to the Sun. Both lead to a larger fraction of stars with large $\langle S_{ph} \rangle$ and consequently $\sigma(S_{ph})$. The L bias is however expected as low L stars (less evolved) are the most numerous in the full sample, which can be seen for example in the density of gray data points in the background. We find a moderate negative correlation between the residual $\langle S_{ph} \rangle$ and L (Table 2). Simultaneously, the Sun-like sample has more stars rotating slightly faster than stars rotating more slowly than the Sun. This is an expected bias as the P_{rot} distribution for *Kepler* G dwarfs peaks around 20 days (see Appendix B.4). P_{rot} and $\langle S_{ph} \rangle$ are strongly correlated (Table 2), with activity increasing toward fast rotation (negative correlation). It is important to note that the measured P_{rot} depends on the (unknown) spot latitudes in a differentially rotating star, and thus the P_{rot} is interpreted as an average value of the surface rotation. In summary, the T_{eff}, L, and P_{rot} biases in the sample of Sun-like stars would lead to a bias toward higher activity levels than the Sun. Nevertheless, we still find the $S_{ph\odot}$ to be consistent with that of the selected Sun-like stars (see below). Finally, we also find a weak correlation between metallicity and $\langle S_{ph} \rangle$ (Table 2).

Figure 8 shows the comparison between the cumulative distribution functions (CDFs) of the residuals for the Sun (blue solid line) and the Sun-like stars (red shaded region). Concerning the average magnetic activity (left), the distribution of the log $\langle S_{ph\odot} \rangle$ residuals is consistent with that of Sun-like stars. The p-value from the Kolmogorov-Smirnov test (Kolmogorov 1933; Smirnov 1939) is 0.30, which supports the null hypothesis of the two samples ($\langle S_{ph\odot} \rangle$ and $\langle S_{ph} \rangle$ for *Kepler* Sun-like stars) were
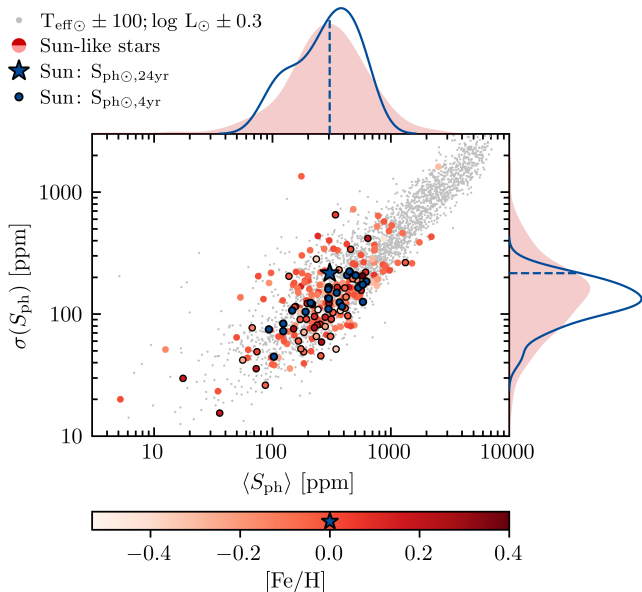
Fig. 7. $\sigma(S_{\mathrm{ph}})$ as a function of $\langle S_{\mathrm{ph}} \rangle$ for the Sun and the Sun-like stars. For reference, the gray dots show the G dwarfs with similar T_{eff} and L, but any P_{rot}. The Sun-like stars are indicated in red, and the shade represents the metallicity. The respective distributions are shown in red on the top and right panels. The outlined targets have spectroscopic parameters. The results from the 4 yr VIRGO g+r segments are shown with the blue circles, and the respective distributions are shown with the solid blue line. The blue star in the main panel and the dashed blue lines correspond to the full light curve, and the blue star in the color bar indicates solar metallicity.

drawn from the same distribution. The comparison between the two CDFs also illustrates that there are more stars with low and high activity than the Sun had epochs of such low or high activity during the past two cycles. Concerning the variation of the magnetic activity, the results for the Sun and the Sun-like stars are also consistent (p-value of 0.11). However, there is a larger fraction of highly variable stars in comparison with the variability of the $S_{\mathrm{ph}\odot}$.
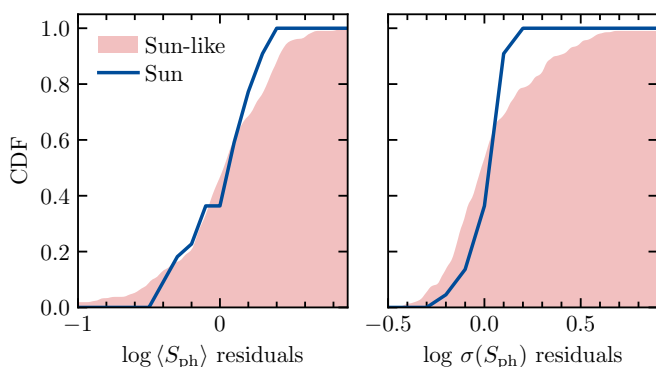

Fig. 8. CDF for the log $\langle S_{\mathrm{ph}} \rangle$ and log $\sigma(S_{\mathrm{ph}})$ residuals for the Sun-like stars (red shaded region) and the Sun (solid blue line).

4.4. Doris and the Doris-like stars

In this section we compare Doris (KIC 8006161) with the Doris-like stars. Doris usually stands out when compared with other

solar-like stars (namely FGK dwarfs; e.g., Karoff et al. 2018; Santos et al. 2019a). Its peculiar behavior has been attributed to its high metallicity, which changes the opacity and depth of the convection zone and, thus, affects magnetic activity. Above, for the stars with similar T_{eff} and L to the Sun, we already found evidence for a weak correlation between [Fe/H] and $\langle S_{\mathrm{ph}} \rangle$. Here, we selected the Doris-like stars by implementing the same criteria as in the previous section, but based on the stellar properties of Doris: $T_{\mathrm{eff, Doris}} = 5488$ K; $L_{\mathrm{Doris}} = 0.67\,L_\odot$; and $P_{\mathrm{rot, Doris}} = 31.71$ days (Berger et al. 2020; Santos et al. 2021a). These selection criteria lead to a subsample of 173 Doris-like stars. Figure 9 shows the HR diagram highlighting Doris and the Doris-like stars. The Doris-like stars are more uniformly distributed in T_{eff} than the Sun-like stars, but are still biased toward low L. Similarly to the previous section, most of the Doris-like stars are rotating slightly faster than Doris, according to their average rotation periods (Appendix B.4).
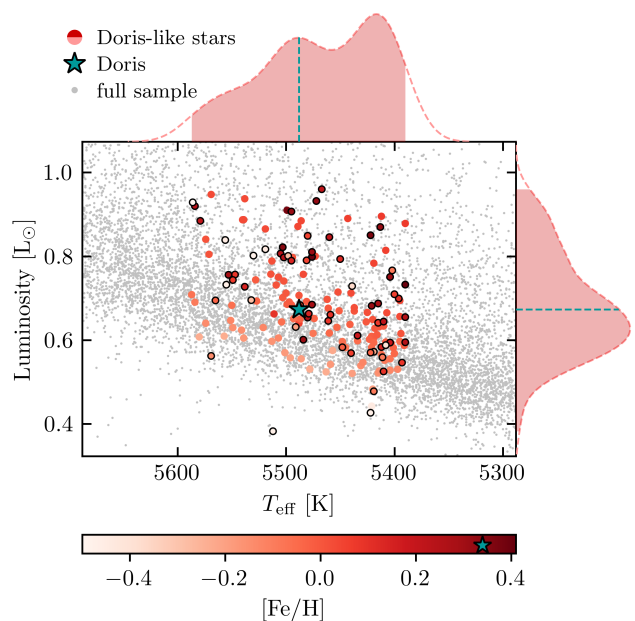

Fig. 9. Same as in Fig. 6 but for Doris and Doris-like stars.

The comparison between Doris and the Doris-like stars is shown in Fig. 10. The 4-year average and standard deviation of S_{ph} for Doris are marked by the turquoise star. The turquoise line indicates the minimum and maximum individual S_{ph} values. The Doris-like stars are marked in shades of red, which indicate the metallicity of the targets. Interestingly, Doris-like stars seem to be more metallic than the full G dwarf sample.

When compared with stars with very similar properties, Doris is not an outlier. Nevertheless, Doris is still among the most active and most variable stars: 79% of the Doris-like stars have a $\langle S_{\mathrm{ph}} \rangle$ value smaller than $\langle S_{\mathrm{ph}} \rangle_{\mathrm{Doris}}$; and 76% of the Doris-like stars have a $\sigma(S_{\mathrm{ph}})$ value smaller than $\sigma(S_{\mathrm{ph}})_{\mathrm{Doris}}$. The lowest S_{ph} value observed by *Kepler* is still consistent with high activity. Indeed *Kepler* observations started at the minimum of activity between two cycles (Karoff et al. 2018).

We perform the multivariate regression based on all targets in gray (similar T_{eff} and L to those of Doris) and compute the correlation coefficients for the isolated dependences (Table 3). Particularly, the results are consistent with a weak correlation between the $\langle S_{\mathrm{ph}} \rangle$ and [Fe/H]. The evidence for a correlation between $\langle S_{\mathrm{ph}} \rangle$ and [Fe/H] (here and in the previous section) sup-

ports the interpretation by Karoff et al. (2018, see also See et al. 2021) for Doris's strong magnetic activity.
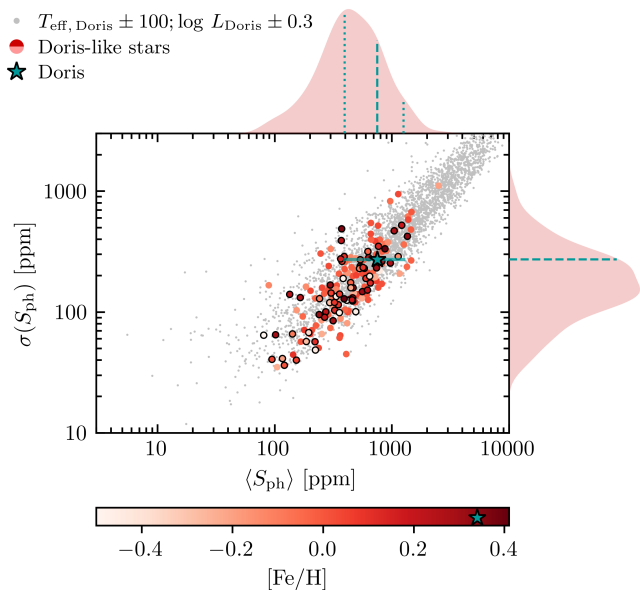

Fig. 10. Same as in Fig. 7 but for Doris and Doris-like stars. Doris is marked in turquoise, as in Fig. 2. The dashed lines mark the $\langle S_{\rm ph} \rangle$ and $\sigma(S_{\rm ph})$ for Doris, and the dotted lines mark the maximum and minimum $S_{\rm ph}$ values (also indicated in the main panel by the horizontal line). In the color bar, the turquoise star marks the metallicity of Doris.

Fig. 11. $P_{\rm rot}$ distributions for metal poor (left), solar metallicity (middle), and metal rich (right) stars within 100K to the $T_{\rm eff}$ of the Sun (top) and Doris (bottom). Dark red shows the distribution for all stars, while light red corresponds to those with spectroscopic parameters. We only consider main-sequence stars. The shaded regions in blue and turquoise mark the $P_{\rm rot}$ interval used to select Sun-like and Doris-like stars. The white circles indicate the median values, while the black bars indicate the 1$^{\rm st}$ and 3$^{\rm rd}$ quartiles of the distributions.

4.5. Relation between P_{rot} and metallicity

Focusing solely on spectroscopic APOGEE and LAMOST metallicities for the *Kepler* stars, Amard et al. (2020) found that metal-rich stars are systematically slower rotators (from McQuillan et al. 2014) than their metal-poor counterparts.

The first evidence in our sample for such a relation between $P_{\rm rot}$ and [Fe/H] is found among the Doris-like stars, which were selected according to their $T_{\rm eff}$, L, and $P_{\rm rot}$. In the resulting sample, there is an excess of metal-rich stars in comparison to the full G-dwarf sample (see Appendix B.4). This suggests that metallicity may play an important role in generating such slow rotators ($P_{\rm rot} \sim 31$ days) in this region of the HR diagram.

Figure 11 shows the $P_{\rm rot}$ distributions for the Sun-like and Doris-like stars split according to their metallicity. We consider three [Fe/H] intervals: metal poor [Fe/H] ≤ -0.2; solar metallicity $-0.2 <$ [Fe/H] < 0.2; and metal rich [Fe/H] ≥ 0.2. The blue and turquoise shaded regions mark the interval of Sun-like and Doris-like $P_{\rm rot}$, respectively. In the parameter space of the Sun-like stars, the $P_{\rm rot}$ distributions are similar for all [Fe/H] intervals. In the Doris-like $T_{\rm eff}$ regime, the $P_{\rm rot}$ distribution shifts toward longer $P_{\rm rot}$ for the metal-rich subsample in comparison to the metal-poor and solar-metallicity ones.

A detailed investigation of the relationship between $P_{\rm rot}$ and metallicity is beyond the scope of the current study. The impact of metallicity in the magnetic-activity and rotational evolution will be the focus of a future work. Nevertheless, the goal of this section was to verify the source of the excess of metal-rich stars in the Doris-like sample. Particularly, in the context of Doris being a metal-rich star, whose metal content may be behind its strong activity. Above, we confirm that, in the Doris-like $T_{\rm eff}$, the metal-rich stars are indeed slower rotators than the remain-
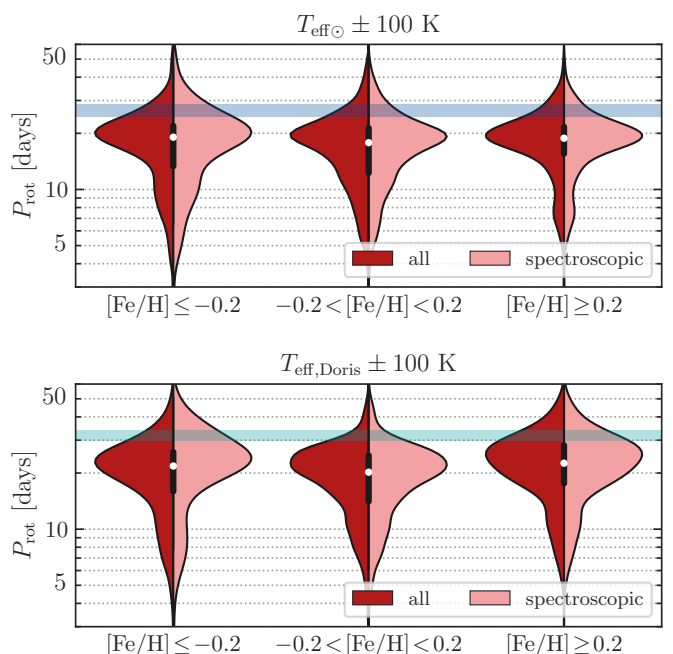
der. These results support the dependence of $P_{\rm rot}$ on [Fe/H] found by Amard et al. (2020).

5. Discussion and conclusions

With the advent of planet-hunting missions such as *Kepler*, high-precision photometric time series are available for an extraordinarily large number of solar-like stars. For time series with rotational modulation, the photometric magnetic activity can be constrained through the $S_{\rm ph}$ (Mathur et al. 2014). In this work we investigate the temporal variability of the $S_{\rm ph}$ over the length of the *Kepler* observations. Our target sample includes more than 44,000 *Kepler* solar-like (FGKM) stars with known average surface rotation periods and average $S_{\rm ph}$ (selected from Santos et al. 2019b, 2021a). Furthermore, we analyzed solar VIRGO/SPM data in order to compare the behavior of the solar $S_{\rm ph}$ with that observed for other stars.

We find that the photometric magnetic activity is more variable for stars that are on average more active in comparison to that of weakly active targets. This kind of relationship is known for the chromospheric magnetic activity (e.g., Wilson 1978; Radick et al. 1998; Lockwood et al. 2007; Egeland 2017; Gomes da Silva et al. 2021; Brown et al. 2022) and surface-averaged magnetic field strength (Brown et al. 2022), but in this work we show that it is also observed in the *Kepler* photometric data of solar-like stars. In particular, the standard deviation of the individual measurements of photometric magnetic activity, $\sigma(S_{\rm ph})$, and their average value, $\langle S_{\rm ph} \rangle$, are very strongly correlated, independent of the spectral type. This includes the low-activity fast-rotating F stars. Due to their thin convective zones, for most of the main sequence, F stars have longer spin-down

		main sequence				
		M	K	G	F	subgiant
	N stars	426	13,499	20,235	7,771	2,674
	$\langle S_{\rm ph}\rangle_{\rm 5th}$	567.1	281.7	81.4	30.9	37.4
	$\langle S_{\rm ph}\rangle_{\rm 95th}$	5950.6	5125.5	4870.7	2031.6	4239.8
	Kp	0.07	0.07	0.15	0.28	0.21
	$t_{\rm obs}$	0.00	-0.09	-0.12	-0.20	-0.17
	$T_{\rm eff}$	0.11	0.10	-0.07	-0.14	-0.24
SCC	L	-0.11	0.00	-0.11	-0.15	0.04
	[Fe/H]	0.03	0.04	0.01	-0.06	-0.02
	$P_{\rm rot}$	-0.38	-0.36	-0.37	-0.15	-0.16
	$\langle S_{\rm ph}\rangle$	0.84	0.91	0.94	0.88	0.88

FAST-ROTATING POPULATION

		M	K	G
	N stars	175	2,848	2,104
	$\langle S_{\rm ph}\rangle_{\rm 5th}$	507.8	378.8	138.7
	$\langle S_{\rm ph}\rangle_{\rm 95th}$	7624.7	9666.7	6800.0
	Kp	0.06	0.06	0.02
	$t_{\rm obs}$	-0.05	-0.15	-0.15
	$T_{\rm eff}$	0.16	-0.03	-0.07
SCC	L	-0.11	0.01	-0.07
	[Fe/H]	0.12	0.07	0.01
	$P_{\rm rot}$	-0.46	-0.41	-0.19
	$S_{\rm ph}$	0.91	0.93	0.93

SLOW-ROTATING POPULATION

		M	K	G
	N stars	251	10,651	18,131
	$\langle S_{\rm ph}\rangle_{\rm 5th}$	742.5	269.1	78.1
	$\langle S_{\rm ph}\rangle_{\rm 95th}$	4518.0	4465.6	4410.3
	Kp	0.08	0.08	0.16
	$t_{\rm obs}$	0.01	-0.08	-0.12
	$T_{\rm eff}$	0.18	0.07	-0.06
SCC	L	-0.26	0.00	-0.12
	[Fe/H]	0.03	0.04	0.02
	$P_{\rm rot}$	-0.18	-0.35	-0.33
	$\langle S_{\rm ph}\rangle$	0.77	0.89	0.93

Table 1. Spearman correlation coefficients (SCCs) between the log $\sigma(S_{\rm ph})$ residuals, when isolating each dependence, and the different observational and stellar properties. The first part of the table concerns all the stars in Fig. 2, which are split into slow- and fast-rotating populations (GKM) for the second and third parts of the table (Fig. 4). The top lines of each part indicate the number of stars and 5th and 95th percentiles of the $\langle S_{\rm ph}\rangle$ distribution.

	$T_{\rm eff\odot} \pm 100$ K; $L_\odot \pm 0.3$		
		all	spectroscopic
	N stars	3470	1303
	$\langle S_{\rm ph}\rangle_{\rm 5th}$	87.0	72.0
	$\langle S_{\rm ph}\rangle_{\rm 95th}$	4454.6	4552.9

		$\langle S_{\rm ph}\rangle$	$\sigma(S_{\rm ph})$	$\langle S_{\rm ph}\rangle$	$\sigma(S_{\rm ph})$
	$T_{\rm eff}$	0.03	-0.02	-0.04	-0.03
	L	-0.35	-0.10	-0.28	-0.13
SCC	[Fe/H]	0.20	0.02	0.34	0.11
	$P_{\rm rot}$	-0.67	-0.37	-0.75	-0.38
	$\langle S_{\rm ph}\rangle$	–	0.92	–	0.94

Table 2. SCC between the log $\langle S_{\rm ph}\rangle$ and log $\sigma(S_{\rm ph})$ residuals and the different stellar properties of stars with similar $T_{\rm eff}$ and L to those of the Sun (gray dots in Fig. 8). The first columns correspond to all stars within the parameter space, while the last ones correspond solely to the stars with spectroscopy. The top lines indicate the number of stars and 5th and 95th percentiles of the $\langle S_{\rm ph}\rangle$ distribution.

	$T_{\rm eff,Doris} \pm 100$ K; $L_{\rm Doris} \pm 0.3$		
		all	spectroscopic
	N stars	4240	1443
	$\langle S_{\rm ph}\rangle_{\rm 5th}$	140.9	121.0
	$\langle S_{\rm ph}\rangle_{\rm 95th}$	5208.2	5496.2

		$\langle S_{\rm ph}\rangle$	$\sigma(S_{\rm ph})$	$\langle S_{\rm ph}\rangle$	$\sigma(S_{\rm ph})$
	$T_{\rm eff}$	0.02	-0.02	0.02	-0.01
	L	-0.29	-0.06	0.28	-0.08
SCC	[Fe/H]	0.20	0.00	0.30	0.07
	$P_{\rm rot}$	-0.61	-0.39	-0.65	-0.37
	$\langle S_{\rm ph}\rangle$	–	0.93	–	0.95

Table 3. Same as Table 2 but for stars with $T_{\rm eff}$ and L similar to those of Doris (gray dots in Fig. 10).

timescales in comparison to the lower-mass stars (van Saders & Pinsonneault 2013; Matt et al. 2015) and, thus, do not spin down significantly, remaining fast rotators. Nevertheless, for F stars, there is still a very strong correlation between their average magnetic activity and its variation. We also find such a strong correlation for the subgiant stars that already evolved off the main sequence.

Given that the definition of $S_{\rm ph}$, $\sigma(S_{\rm ph})$ is a measurement of the magnetic activity variability at timescales longer than $P_{\rm rot}$. In particular, as seen for the solar data, $\sigma(S_{\rm ph\odot})$ shows the signature of the long-term 11 yr cycle as well as the signature of the QBOs (short-term variations) at high-activity epochs. From the long-term ground-based spectroscopic observations, several other solar-like stars are known to have variations analogous to the solar QBOs as well as to the long-term activity cycle (e.g., Baliunas et al. 1995; Metcalfe et al. 2013; Egeland et al. 2015). Thus, it is possible that the 4 yr $\sigma(S_{\rm ph})$ for *Kepler* stars also include the signature of both short-term and long-term variations in the magnetic activity.

In addition to the very strong correlation between $\sigma(S_{\rm ph})$ and $\langle S_{\rm ph}\rangle$, our results suggest an additional dependence of the $\sigma(S_{\rm ph})$

on the rotation period, even after accounting for the dependence on $\langle S_{\rm ph}\rangle$. Although the results are only consistent with a weak correlation, at fixed $\langle S_{\rm ph}\rangle$ faster rotators tend to exhibit more magnetic activity variability than slow rotators.

GKM dwarfs in the *Kepler* field fall into two populations, separated by the so-called intermediate-$P_{\rm rot}$ gap, which is especially prominent for K and M dwarfs. For G stars, the $P_{\rm rot}$ distribution is still bimodal, but there is no clear gap (Appendix B.3). While the fast-rotating population is on average more active than the slow-rotating one, we find that the distributions of the $\sigma(S_{\rm ph})$ residuals (computed using a multivariate regression) are similar for both populations. These results suggest that the relation between the mean value of $S_{\rm ph}$ and its variability does not change.

The Sun also follows the same $\sigma(S_{\rm ph})$ versus $\langle S_{\rm ph}\rangle$ relationship as the other solar-like stars, both for the full 24 yr time series and for the multiple 4 yr segments. The measured values for the solar 4 yr segments illustrate, however, the limitations associated with the observation length. In particular, the 4 yr data points span a relatively wide range of values in both $\sigma(S_{\rm ph})$ and $\langle S_{\rm ph}\rangle$, depending on the phase of the cycle. Four years of *Kepler* continuum monitoring might still be too short in the context of fully characterizing magnetic activity. This is especially important for the slow rotators, whose magnetic activity is expected to vary over longer timescales in comparison to the fast rotators (e.g., Brandenburg et al. 1998; Böhm-Vitense 2007). Moreover, some scatter in the $\sigma(S_{\rm ph})$ versus $\langle S_{\rm ph}\rangle$ can also be introduced by the impact of stellar inclination and spot or active-region latitudes on the amplitude of the rotational signal. In addition to the Sun, we also highlight four other stars: three with cycle candidates

(KIC 5184732, KIC 7970740, and KIC 10644253; Salabert et al. 2016b; Santos et al. 2018) and KIC 8006161 (HD 173701), also known as Doris. Doris is a well-characterized seismic G dwarf with a relatively strong magnetic activity and a confirmed activity cycle of $\sim$ 8 years (Karoff et al. 2018). All these solar-like stars behave in accordance to the general trend.

While the Sun is found to be among the less active and less variable G dwarfs observed by *Kepler*, when compared with Sun-like stars, selected from a very narrow parameter space around the solar properties, the Sun is rather normal. This conclusion is in contrast with the findings by Reinhold et al. (2020), who find that *Kepler* Sun-like stars are distinctively more active than the Sun. We must note, however, that the sample of Sun-like stars with known rotation periods has been extended since then (Santos et al. 2021a). Moreover, the stellar properties adopted to select the Sun-like stars were also updated. As a result, the stellar classification has slightly changed (Appendix B.4). Finally, Metcalfe & van Saders (2020) already noticed possible selection biases.

Similarly to the Sun versus Sun-like stars comparison, we compare the well-characterized G dwarf Doris with Doris-like stars. It has been suggested that its strong magnetic activity is related to its high metal content (Karoff et al. 2018). Our results show that Doris behaves consistently with stars of very similar properties. Nevertheless, Doris is indeed among the most active stars, even at its minimum activity. Interestingly, we find an excess of metal-rich stars among the sample of Doris-like stars (Doris also being a metal-rich star). From the adopted selection criteria, the parameter that could lead to such a peculiar feature in the [Fe/H] distribution is $P_{\rm rot}$. Doris is a slow rotator with $P_{\rm rot} \sim 31.71$ days. Indeed we find that, at $\sim T_{\rm eff,Doris}$, the $P_{\rm rot}$ distribution shifts toward longer values from the metal-poor subsample to the metal-rich subsample. These results are in agreement with the findings by Amard et al. (2020), who also find a $P_{\rm rot}$-[Fe/H] dependence. Furthermore, although Doris is not an activity outlier in comparison to Doris-like stars[5], we find that [Fe/H] still plays a role: Doris-like stars tend to be more metallic; and we find a weak correlation between [Fe/H] and $\langle S_{\rm ph}\rangle$. In fact, our results are consistent with the interpretation proposed in Karoff et al. (2018). Karoff et al. (2018) suggested that Doris's strong magnetic activity is related to a deeper convection zone due to the increased opacity resulting from its high metal content (e.g., Schwarzschild 1906; van Saders & Pinsonneault 2012; Amard & Matt 2020) in comparison to a metal-poor counterpart. If the magnetic activity is stronger, then the magnetic braking and the spin-down will be more efficient, leading to longer rotation periods for a given stellar age. These results are also in good agreement with the theoretical predictions by Amard & Matt (2020), who find a significant [Fe/H] impact on the stellar structure, consistent with metal-rich stars being more magnetically active and spinning down faster than metal-poor stars. In that way, it is important to consider chemical composition in gyrochronology studies (Amard & Matt 2020; Claytor et al. 2020a).

Finally, we note that the *Kepler* $S_{\rm ph}$ data do not show a discontinuity or evidence for a gap in activity that would be consistent with the VP gap, which would be located in the slow-rotating population. However, we consider that *Kepler* $S_{\rm ph}$ data cannot reject the existence of the VP gap, still debated in the literature. Firstly, while photometric and chromospheric APs are

well correlated (Salabert et al. 2016a, 2017), they are sensitive to different activity-related phenomena and to different layers of the stellar atmosphere. Moreover, as shown for the Sun, $\sigma(S_{\rm ph})$ and $\langle S_{\rm ph}\rangle$ values depend on the phase of the cycle. This indicates that we can expect some scatter in the $\sigma(S_{\rm ph})$ versus $\langle S_{\rm ph}\rangle$ relation due to the limited 4 yr *Kepler* observations. This effect, together with the fact that the *Kepler* sample is many times larger than those in chromospheric activity studies, can smear the existence of a lower density region or gap. Thus, our results do not exclude the existence of the VP gap.

References

Agüeros, M. A., Covey, K. R., Lemonias, J. J., et al. 2011, ApJ, 740, 110
Ahumada, R., Prieto, C. A., Almeida, A., et al. 2020, ApJS, 249, 3
Amard, L. & Matt, S. P. 2020, ApJ, 889, 108
Amard, L., Roquette, J., & Matt, S. P. 2020, MNRAS, 499, 3481
Angus, R., Beane, A., Price-Whelan, A. M., et al. 2020, AJ, 160, 90
Astropy Collaboration, Price-Whelan, A. M., Sipőcz, B. M., et al. 2018, AJ, 156, 123
Astropy Collaboration, Robitaille, T. P., Tollerud, E. J., et al. 2013, A&A, 558, A33
Baliunas, S. L., Donahue, R. A., Soon, W. H., et al. 1995, ApJ, 438, 269
Baliunas, S. L., Hartmann, L., Noyes, R. W., et al. 1983, ApJ, 275, 752
Barnes, S. A. 2003, ApJ, 586, 464
Barnes, S. A. 2007, ApJ, 669, 1167
Basri, G., Walkowicz, L. M., Batalha, N., et al. 2010, ApJL, 713, L155
Bazilevskaya, G., Broomhall, A.-M., Elsworth, Y., & Nakariakov, V. M. 2014, Space Sci. Rev., 186, 359
Berger, T. A., Huber, D., Gaidos, E., & van Saders, J. L. 2018, ApJ, 866, 99
Berger, T. A., Huber, D., van Saders, J. L., et al. 2020, AJ, 159, 280
Borucki, W. J., Koch, D., Basri, G., et al. 2010, Science, 327, 977
Boyle, A. W. & Bouma, L. G. 2022, arXiv:2211.09822
Brandenburg, A., Saar, S. H., & Turpin, C. R. 1998, ApJL, 498, L51
Breton, S. N., Santos, A. R. G., Bugnet, L., et al. 2021, A&A, 647, A125
Broomhall, A.-M., Chaplin, W. J., Elsworth, Y., & Simoniello, R. 2012, MNRAS, 420, 1405
Broomhall, A.-M. & Nakariakov, V. M. 2015, Sol. Phys., 290, 3095
Brown, E. L., Jeffers, S. V., Marsden, S. C., et al. 2022, MNRAS, 514, 4300
Brun, A. S. & Browning, M. K. 2017, Living Rev. Solar Phys., 14, 4
Böhm-Vitense, E. 2007, ApJ, 657, 486
Ceillier, T., Tayar, J., Mathur, S., et al. 2017, A&A, 605, A111
Ceillier, T., van Saders, J., García, R. A., et al. 2016, MNRAS, 456, 119
Claytor, Z. R., van Saders, J. L., Santos, A. R. G., et al. 2020a, ApJ, 888, 43

---

[5] Doris is found to be an activity outlier in comparison to stars within a broader parameter space than that adopted in this study (e.g., Kiefer et al. 2017; Karoff et al. 2018; Santos et al. 2019a).

Claytor, Z. R., van Saders, J. L., Santos, A. R. G., et al. 2020b, Astrophysics Source Code Library, ascl:2011.027
Covington, A. E. 1969, J. R. Astron. Soc. Canada, 63, 125
Davenport, J. R. A. & Covey, K. R. 2018, ApJ, 868, 151
Domingo, V., Fleck, B., & Poland, A. I. 1995, Sol. Phys., 162, 1
Egeland, R. 2017, Ph.D. Thesis
Egeland, R., Metcalfe, T. S., Hall, J. C., & Henry, G. W. 2015, ApJ, 812, 12
Fritzewski, D. J., Barnes, S. A., James, D. J., Järvinen, S. P., & Strassmeier, K. G. 2021, A&A, 656, A103
Fröhlich, C., Andersen, B. N., Appourchaux, T., et al. 1997, Sol. Phys., 170, 1
Fröhlich, C., Romero, J., Roth, H., et al. 1995, Sol. Phys., 162, 101
Furlan, E., Ciardi, D. R., Cochran, W. D., et al. 2018, ApJ, 861, 149
Gaia Collaboration, Arenou, F., Babusiaux, C., et al. 2022, Gaia Data Release 3: Stellar multiplicity, a teaser for the hidden treasure, Tech. rep.
Gaia Collaboration, Brown, A. G. A., Vallenari, A., Prusti, T., et al. 2021, A&A, 649, A1
Gaia Collaboration, Prusti, T., Bruijne, J. H. J. d., Brown, A. G. A., et al. 2016, A&A, 595, A1
García, R. A., Ceillier, T., Salabert, D., et al. 2014a, A&A, 572, A34
García, R. A., Hekker, S., Stello, D., et al. 2011, MNRAS, 414, L6
García, R. A., Mathur, S., Pires, S., et al. 2014b, A&A, 568, A10
García, R. A., Mathur, S., Salabert, D., et al. 2010, Science, 329, 1032
Giles, H. A. C., Collier Cameron, A., & Haywood, R. D. 2017, MNRAS, 472, 1618
Gomes da Silva, J., Santos, N. C., Adibekyan, V., et al. 2021, A&A, 646, A77
Gordon, T. A., Davenport, J. R. A., Angus, R., et al. 2021, ApJ, 913, 70
Gustafsson, B. 1998, SSR, 85, 419
Henry, T. J., Soderblom, D. R., Donahue, R. A., & Baliunas, S. L. 1996, AJ, 111, 439
Howell, S. B., Sobeck, C., Haas, M., et al. 2014, PASP, 126, 398
Hunter, J. D. 2007, Computing in Science & Engineering, 9, 90
Jain, K., Tripathy, S. C., & Hill, F. 2009, ApJ, 695, 1567
Jenkins, J. M., Caldwell, D. A., Chandrasekaran, H., et al. 2010, ApJ, 713, L120
Jiménez, A., Roca Cortés, T., & Jiménez-Reyes, S. J. 2002, Sol. Phys., 209, 247
Jones, E., Oliphant, T., Peterson, P., et al. 2001–, SciPy: Open source scientific tools for Python
Karoff, C., Metcalfe, T. S., Santos, A. R. G., et al. 2018, ApJ, 852, 46
Kawaler, S. D. 1988, ApJ, 333, 236
Kiefer, R., Schad, A., Davies, G., & Roth, M. 2017, A&A, 598, A77
Kolmogorov, A. N. 1933, Giornale dell'Istituto Italiano degli Attuari, 4, 83
Kraft, R. P. 1967, ApJ, 150, 551
Lanza, A. F., Das Chagas, M. L., & De Medeiros, J. R. 2014, A&A, 564, A50
Lindegren, L., Klioner, S. A., Hernández, J., et al. 2021, A&A, 649, A2
Lockwood, G. W., Skiff, B. A., Baliunas, S. L., & Radick, R. R. 1992, Nature, 360, 653
Lockwood, G. W., Skiff, B. A., Henry, G. W., et al. 2007, ApJS, 171, 260
Lu, Y. L., Curtis, J. L., Angus, R., David, T. J., & Hattori, S. 2022, AJ, 164, 251
Lund, M. N., Silva Aguirre, V., Davies, G. R., et al. 2017, ApJ, 835, 172
Mathur, S., García, R. A., Ballot, J., et al. 2014, A&A, 562, A124
Mathur, S., García, R. A., Régulo, C., et al. 2010, A&A, 511, A46
Mathur, S., Huber, D., Batalha, N. M., et al. 2017, ApJS, 229, 30
Matt, S. P., Brun, A. S., Baraffe, I., Bouvier, J., & Chabrier, G. 2015, ApJ, 799, L23
McQuillan, A., Mazeh, T., & Aigrain, S. 2013, ApJ, 775, L11
McQuillan, A., Mazeh, T., & Aigrain, S. 2014, ApJS, 211, 24
Mehta, T., Jain, K., Tripathy, S. C., et al. 2022, MNRAS, 515, 2415
Metcalfe, T. S., Buccino, A. P., Brown, B. P., et al. 2013, ApJL, 763, L26
Metcalfe, T. S. & van Saders, J. 2020, Comment on "The Sun is less active than other solar-like stars", Tech. rep., arXiv:2007.04416
Montet, B. T., Tovar, G., & Foreman-Mackey, D. 2017, ApJ, 851, 116
Nielsen, M. B., Gizon, L., Schunker, H., & Karoff, C. 2013, A&A, 557, L10
Noyes, R. W., Hartmann, L. W., Baliunas, S. L., Duncan, D. K., & Vaughan, A. H. 1984, ApJ, 279, 763
pandas development team, T. 2020, pandas-dev/pandas: Pandas, doi:10.5281/zenodo.3509134
Pedregosa, F., Varoquaux, G., Gramfort, A., et al. 2011, Journal of Machine Learning Research, 12, 2825
Pires, S., Mathur, S., García, R. A., et al. 2015, A&A, 574, A18
Radick, R. R., Lockwood, G. W., Henry, G. W., Hall, J. C., & Pevtsov, A. A. 2018, ApJ, 855, 75
Radick, R. R., Lockwood, G. W., Skiff, B. A., & Baliunas, S. L. 1998, ApJS, 118, 239
Rebull, L. M., Stauffer, J. R., Bouvier, J., et al. 2016, AJ, 152, 113
Reiners, A. & Mohanty, S. 2012, ApJ, 746, 43
Reinhold, T., Bell, K. J., Kuszlewicz, J., Hekker, S., & Shapiro, A. I. 2019, A&A, 621, A21
Reinhold, T. & Hekker, S. 2020, A&A, 635, A43
Reinhold, T., Reiners, A., & Basri, G. 2013, A&A, 560, A4

Reinhold, T., Shapiro, A. I., Solanki, S. K., et al. 2020, Science, 368, 518
Salabert, D., García, R. A., Beck, P. G., et al. 2016a, A&A, 596, A31
Salabert, D., García, R. A., Jiménez, A., et al. 2017, A&A, 608, A87
Salabert, D., Régulo, C., García, R. A., et al. 2016b, A&A, 589, A118
Santos, A. R. G., Breton, S. N., Mathur, S., & García, R. A. 2021a, ApJS, 255, 17
Santos, A. R. G., Campante, T. L., Chaplin, W. J., et al. 2018, ApJS, 237, 17
Santos, A. R. G., Campante, T. L., Chaplin, W. J., et al. 2019a, ApJ, 883, 65
Santos, A. R. G., García, R. A., Mathur, S., et al. 2019b, ApJS, 244, 21
Santos, A. R. G., Mathur, S., García, R. A., Cunha, M. S., & Avelino, P. P. 2021b, MNRAS, 508, 267
Schröder, K.-P., Mittag, M., Hempelmann, A., González-Pérez, J. N., & Schmitt, J. H. M. M. 2013, A&A, 554, A50
Schwarzschild, K. 1906, WisGo, 195, 41
See, V., Roquette, J., Amard, L., & Matt, S. P. 2021, ApJ, 912, 127
Silva Aguirre, V., Lund, M. N., Antia, H. M., et al. 2017, ApJ, 835, 173
Simonian, G. V. A., Pinsonneault, M. H., & Terndrup, D. M. 2019, ApJ, 871, 174
Skumanich, A. 1972, ApJ, 171, 565
Smirnov, N. V. 1939, Bulletin Moscow University, 2, 3616
Soderblom, D. R. 1985, AJ, 90, 2103
Soderblom, D. R., Stauffer, J. R., Hudon, J. D., & Jones, B. F. 1993, ApJS, 85, 315
Spada, F. & Lanzafame, A. C. 2020, A&A, 636, A76
Tapping, K. F. 1987, J. Geophys. Res., 92, 829
Tapping, K. F. & Detracey, B. 1990, Sol. Phys., 127, 321
van der Walt, S., Colbert, S. C., & Varoquaux, G. 2011, CiSE, 13, 22
van Saders, J. L., Ceillier, T., Metcalfe, T. S., et al. 2016, Nat., 529, 181
van Saders, J. L. & Pinsonneault, M. H. 2012, ApJ, 746, 16
van Saders, J. L. & Pinsonneault, M. H. 2013, ApJ, 776, 67
Vaughan, A. H. 1980, PASP, 92, 392
Vaughan, A. H., Baliunas, S. L., Middelkoop, F., et al. 1981, ApJ, 250, 276
Vaughan, A. H. & Preston, G. W. 1980, PASP, 92, 385
Waskom, M. L. 2021, Journal of Open Source Software, 6, 3021
Wes McKinney. 2010, in Proceedings of the 9th Python in Science Conference, ed. Stéfan van der Walt & Jarrod Millman, 56 – 61
Wilson, O. C. 1963, ApJ, 138, 832
Wilson, O. C. 1978, ApJ, 226, 379
Wilson, O. C. & Skumanich, A. 1964, ApJ, 140, 1401
Wright, J. T. 2004, ApJ, 128, 1273
Wright, N. J., Drake, J. J., Mamajek, E. E., & Henry, G. W. 2011, ApJ, 743, 48
Zhao, G., Zhao, Y.-H., Chu, Y.-Q., Jing, Y.-P., & Deng, L.-C. 2012, RAA, 12, 723
Zong, W., Fu, J.-N., Cat, P. D., et al. 2020, ApJS, 251, 15

Appendix A: Solar rotation and magnetic activity

In order to compare the Sun with other solar-like stars, we use Sun-as-a-star VIRGO g+r (Sects. 2.1 and 4.1). Here, we summarize the results from the rotational analysis of VIRGO g+r. Figure A.1 shows the VIRGO g+r light curve and the results from the rotation diagnostics employed in our rotation pipeline (e.g., Mathur et al. 2010; García et al. 2014a; Ceillier et al. 2016, 2017).
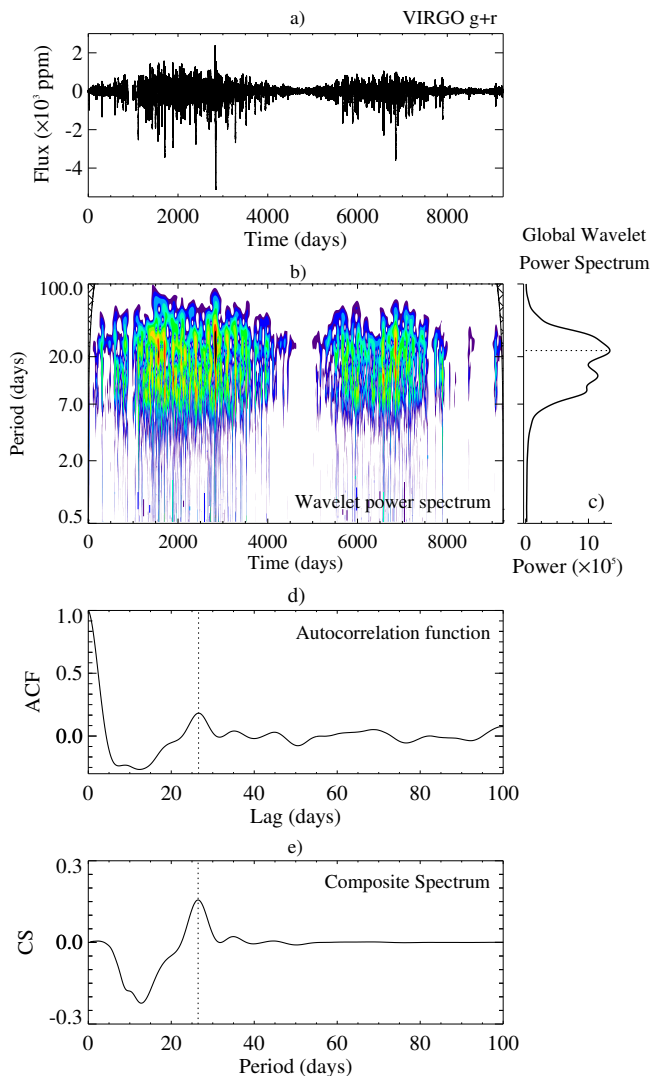

Fig. A.1. Rotational analysis for the Sun. a) Solar VIRGO g+r light curve for more than 24 years, accounting for solar cycles 23 and 24. b) Wavelet power spectrum (WPS), where we adopt the Morlet wavelet. The color code corresponds to Rainbow+White, where black and white correspond to the highest and the lowest power, respectively. c) GWPS, which is the sum of power along the x-axis of the WPS (i.e., time). d) ACF of the light curve. e) CS, which is the product between the normalized versions of c) and d). The dotted lines indicate the three period estimates.

The rotation pipeline employs wavelet analysis, the ACF, and the CS. The latter is indeed the composition between the former two, corresponding to the product of their normalized counterparts. We favor the $P_{\rm rot}$ estimate from the global wavelet power spectrum (GWPS) because of the conservative uncertainty, which for *Kepler* solar-like stars is on average 10% of $P_{\rm rot}$ (Santos et al. 2021a). The ACF and CS serve mostly as validation diagnostics and help prevent the selection of false positives. For example, the ACF is less sensitive to the harmonics of $P_{\rm rot}$

than the wavelet analysis. The CS accentuates common peaks between the ACF and GWPS while attenuating signals that correspond potentially to a harmonic of $P_{\rm rot}$ or that are potentially not related to stellar rotation, for example instrumental artifacts.

The rotation period estimates obtained from the full solar light curve are: $P_{\rm GWPS} = 22.87 \pm 3.47$ d; $P_{\rm ACF} = 26.57$ d, and $P_{\rm CS} = 26.43 \pm 1.04$ d. The $P_{\rm GWPS}$ is short in comparison with the expected rotation at the sunspot latitudes, but the uncertainty is relatively large, and, thus, the expected value is within the error bars. The GWPS (panel b of Fig. A.1) shows a blended band of strong rotational signal ranging roughly from the first to the third harmonics of the rotation period. This results into three broad overlapping peaks in the GWPS. The amplitude of the peaks associated with $P_{\rm ACF}$ and $P_{\rm CS}$ is relatively small. In particular, the fast decay of the ACF suggests short-lived spots or active regions (Lanza et al. 2014; Giles et al. 2017; Santos et al. 2021b), which is known to be the case of the majority of the solar active-regions. In Appendix B.4 we show that the results and comparison between the Sun and the Sun-like stars do not change significantly whether we adopt the $P_{\rm GWPS}$ or $P_{\rm CS}$. Nevertheless, particularly concerning the selection of Sun-like stars, we adopt $P_{\rm rot\odot} = 26.43$ d to compute the $S_{\rm ph}$.

In relation to the rotational analysis of the *Kepler* targets, there is a slight tendency for the GWPS to recover periods that are shorter than those retrieved through the ACF and CS (Fig. A.2). Nevertheless, the difference tends to be small and is encompassed by the uncertainty associated with the GWPS period estimate. Figure A.2 shows the distribution of the ratio between the $P_{\rm ACF}$ or $P_{\rm CS}$ (where "cand" stands for candidate) and the final $P_{\rm rot}$ from Santos et al. (2019b, 2021a), being that $P_{\rm rot}$ mostly corresponds to the $P_{\rm GWPS}$. Figure A.2 illustrates the reliability of the GWPS estimates in Santos et al. (2019b, 2021a) as the difference between the different period estimates is on average small and differences as great as that of the Sun are not common.
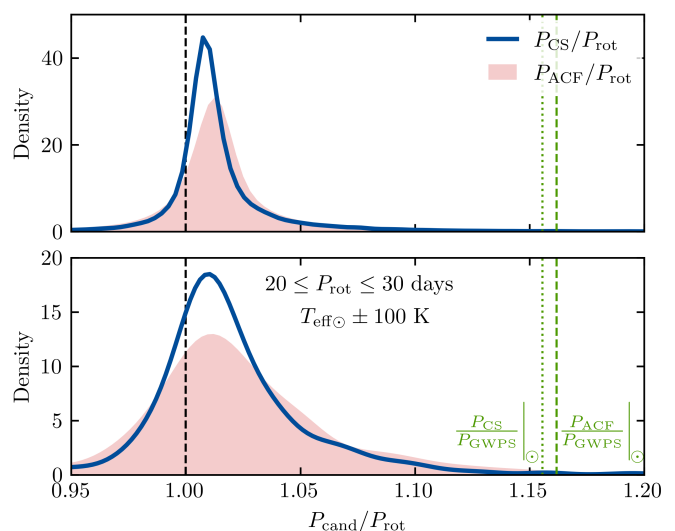
Fig. A.2. Distribution of the ratio between the $P_{\rm ACF}$ (red shaded region) or $P_{\rm CS}$ (solid blue line) and the final $P_{\rm rot}$ for *Kepler* solar-like stars (Santos et al. 2019b, 2021a), where "cand" stands for period candidate. The top panel corresponds to all stars where $P_{\rm cand}$ are within 30% with respect to $P_{\rm rot}$. The bottom panel highlights the stars with $P_{\rm rot}$ estimates within 20 and 30 days and $T_{\rm eff}$ around $T_{\rm eff\odot}$. The black dashed line marks $P_{\rm cand}/P_{\rm rot} = 1$ and the green dashed and dotted lines indicate the $P_{\rm ACF}/P_{\rm GWPS}$ and $P_{\rm CS}/P_{\rm GWPS}$ for the Sun, respectively.

This verification ensures that there is no bias related to P_{rot} when selecting the Sun-like stars. Furthermore, we correct the $\langle S_{ph} \rangle$ and $\sigma(S_{ph})$ for their dependences on different properties, including P_{rot}. Still, in Appendix B.4, we compare the Sun with a group of stars rotating with periods around P_{GWPS}.

We then compute the $S_{ph\odot}$ over segments of length $5 \times P_{rot\odot}$. Figure A.3 compares the S_{ph} when adopting the P_{GWPS} (red) or P_{CS} (blue; adopted as $P_{rot\odot}$). Since the timescales are very similar, the differences are negligible.
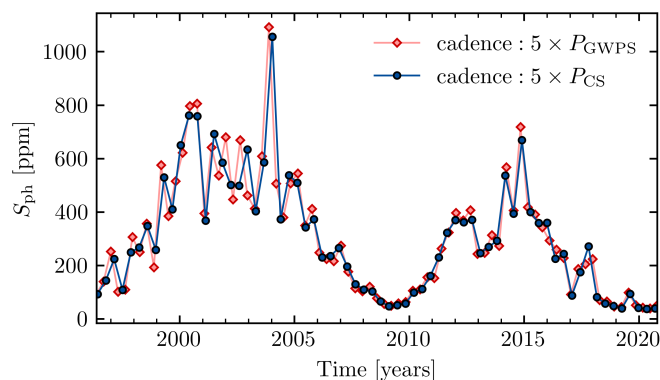

Fig. A.3. Comparison between the solar S_{ph} computed when adopting the P_{GWPS} (red) or P_{CS} (blue). We use the latter as the reference $S_{ph\odot}$.

For comparison and to have access to a more complete picture of the magnetic activity of the present Sun, here we also use the SAs and radio flux ($F_{10.7}$) data, which we re-binned to the same cadence as $S_{ph\odot}$. The re-binning was done by computing the average SA or $F_{10.7}$ over a given time interval of length $5 \times P_{rot\odot}$.

Figure A.4 compares the different magnetic APs with the cadence $5 \times P_{rot\odot}$. It is clear that the re-binned SA (blue) and $F_{10.7}$ (orange) behave more smoothly than the $S_{ph\odot}$. The right-hand side panels of Fig. A.4 show how the different magnetic APs relate to each other for the contemporaneous observations. Each panel also lists the respective SCC. Due to the sensitivity of different APs to different layers of the atmosphere, and different phenomena related to magnetic activity that have different spatial distributions, magnetic hysteresis is observed as different proxies have different "paths" in the rising and declining phases of the cycle (see, e.g., Jain et al. 2009; Salabert et al. 2017). As illustrated in Fig. A.4, the declining phase tends to be faster in the SA and $F_{10.7}$ than in the $S_{ph\odot}$. Nevertheless, the different APs are strongly correlated. Particularly, Salabert et al. (2017) found that $S_{ph\odot}$ best correlated to the SA.

We then split the solar data into 4 yr segments, spaced by one year: 22 $S_{ph\odot}$ segments (Sect. 4.1); 144 SA segments; and 68 $F_{10.7}$ segments. We computed the average SA and $F_{10.7}$. We then scaled $\langle SA \rangle$ and $\langle F_{10.7} \rangle$ to the $\langle S_{ph\odot} \rangle$. The scaling is determined by the solar cycles 23 and 24[6] and then applied to the remainder of the re-binned SA and $F_{10.7}$ time series. The respective standard deviation for each 4 yr segment is then computed from the scaled data. Both average and standard deviation values of the APs are shown in Fig. A.5. For simplification, hereafter, we refer to the scaled SA and $F_{10.7}$ simply as SA and $F_{10.7}$. As the SA and $F_{10.7}$ data were scaled using solar cycles 23 and 24, the amplitude of those cycles approximately match in the different APs. Interestingly, the amplitude of solar cycle 24 is similar in

---

[6] Solar cycle 23 has larger amplitude and deeper minimum than solar cycle 24. Thus, the scaling is in fact ruled by solar cycle 23.

the scaled SA and $F_{10.7}$. However, for the preceding cycles the amplitude in $F_{10.7}$ is systematically smaller than in SA.

We note that the scaling of the APs could also be determined using the smoothed version of the AP by applying a boxcar filter, which is often considered, for example, to remove or isolate short-term variations, namely the QBOs. Similarly to what is seen for the $S_{ph\odot}$ in Sect. 4.1, the signature of the QBO is present in the 4 yr $\sigma(AP)$ around the activity maxima (bottom panel of Fig. A.5).

The right-hand panels of Fig. A.5 show the AP distributions. The dashed lines correspond to the SA and $F_{10.7}$ data solely for solar cycles 23 and 24. While several of the preceding cycles have amplitudes comparable with solar cycles 23 and 24, the top panels also illustrate the fact that the long SA and $F_{10.7}$ records give access to larger amplitude cycles, that is to say, higher activity levels than those seen in the past 24 years. In addition to the signature of the QBO, the variation in the 4 yr AP data also accounts for the 11-year cycle. The distributions of the $\langle SA \rangle$ and $\langle F_{10.7} \rangle$ are shifted toward smaller values (a decrease of $\sim 13\%$ in comparison with the $\langle S_{ph\odot} \rangle$). The slight difference is due to magnetic hysteresis, particularly the declining phases in SA are faster than in $S_{ph\odot}$ (see also Salabert et al. 2017). However, the bias introduced when re-binning SA and $F_{10.7}$ is clear in the comparison between the $\sigma(AP)$ (bottom).

Appendix B: *Kepler* target sample

Appendix B.1: Spectral types and evolutionary stage

We split our main sample into subsamples, according to the spectral type and possible evolutionary stage. We adopted the same T_{eff} cuts for the spectral types as in Santos et al. (2019b, 2021a): at 3700 K, 5200 K, and 6000 K. To split main-sequence and subgiant stars, we adopted the EEP values from Mathur et al. (in prep). The subsamples are illustrated in Fig. B.1 together with the stellar properties source.

Appendix B.2: Removing potential sources of bias

As described in Sect. 2.2, we have neglected targets that may contribute to a bias on our analysis. Here, we show where those targets lie on the $\sigma(S_{ph})$ versus $\langle S_{ph} \rangle$ diagram.

We neglected targets with a light curve shorter than 12 *Kepler* Quarters. The shorter is the light curve, the less complete is the information retrieved on the photometric activity. This selection criterion removes some of the outliers (above and below) in the $\sigma(S_{ph})$ versus $\langle S_{ph} \rangle$ relation (top panel of Fig. B.2).

The light curves of faint stars tend to be noisy. For faint stars, the spot rotational modulation becomes harder to detect and its amplitude, related to the S_{ph}, is affected. For that reason, we removed for this analysis targets with Kp > 16. This selection criterion also removed a significant number of outliers (second panel of Fig. B.2), particularly those lying below the general trend.

Magnetic activity can be affected by binarity. Thus, in addition to all known eclipsing binaries, which were already absent from the rotational analysis (Santos et al. 2019b, 2021a), we removed all binary candidates identified by Berger et al. (2018); Gaia Collaboration et al. (2022, *Gaia* binaries), by Simonian et al. (2019, tidally synchronized binaries), and by Santos et al. (2019b, 2021a, close-in binary candidates). This removed a significant number of targets that follow the $\sigma(S_{ph})$ versus $\langle S_{ph} \rangle$ relationship (third and bottom panels of Fig. B.2), but it also re-
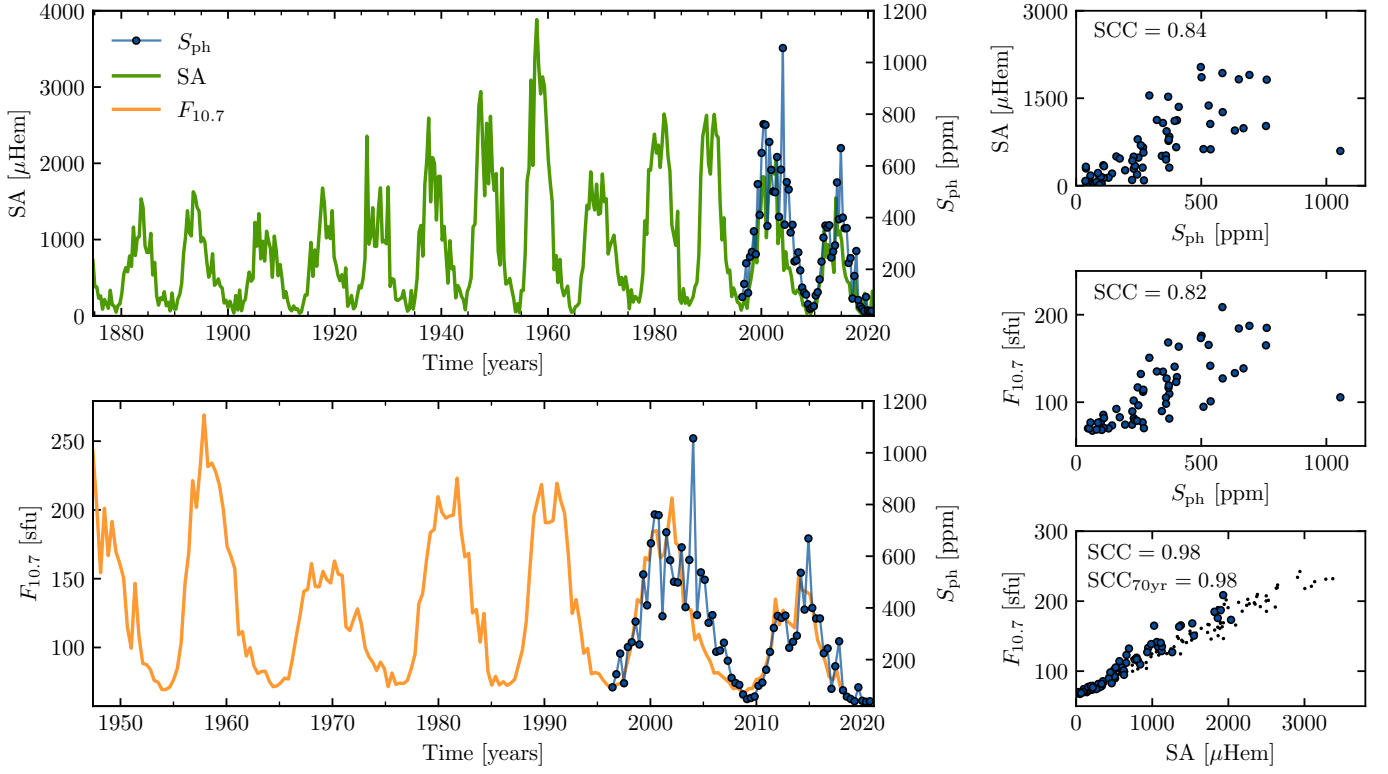
Fig. A.4. Comparison between the solar magnetic APs. In the left panels, S_{ph} from VIRGO g+r is shown by the blue circles, while SA and $F_{10.7}$ are shown by the solid green and orange lines, respectively. The right-hand side shows how $F_{10.7}$, SA, and S_{ph} relate to each other: the blue circles correspond to solar cycles 23 and 24, the black dots correspond to the ~ 70 years of contemporaneous observations of SA and $F_{10.7}$. Each panel shows the corresponding SCC value, where "70yr" stands for 70 years of common SA and $F_{10.7}$ observations.
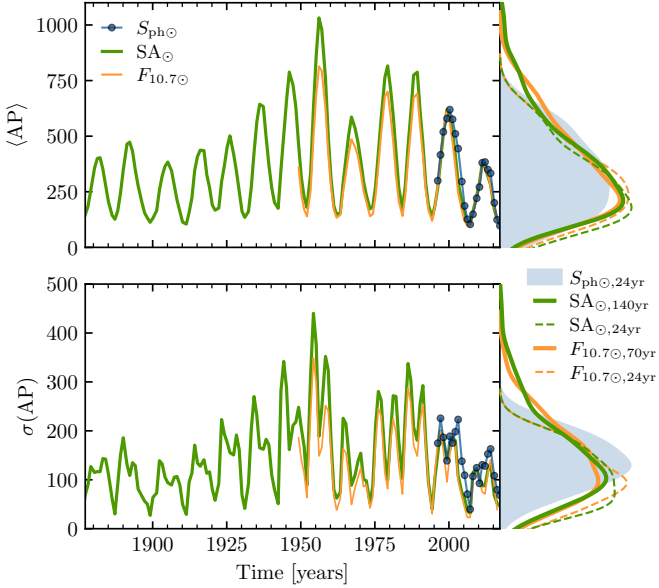
Fig. A.5. Comparison between the average (top) and standard deviation (bottom) values of the APs computed from 4-year segments. In the left panels, the blue symbols correspond to the $S_{ph\odot}$, while the green and orange solid lines concern the scaled SA and $F_{10.7}$, respectively. The right-hand panels show their distributions. "24yr" denotes 24 years, i.e., the two last solar cycles, while "70yr" and "140yr" denote 70 and 140 years.
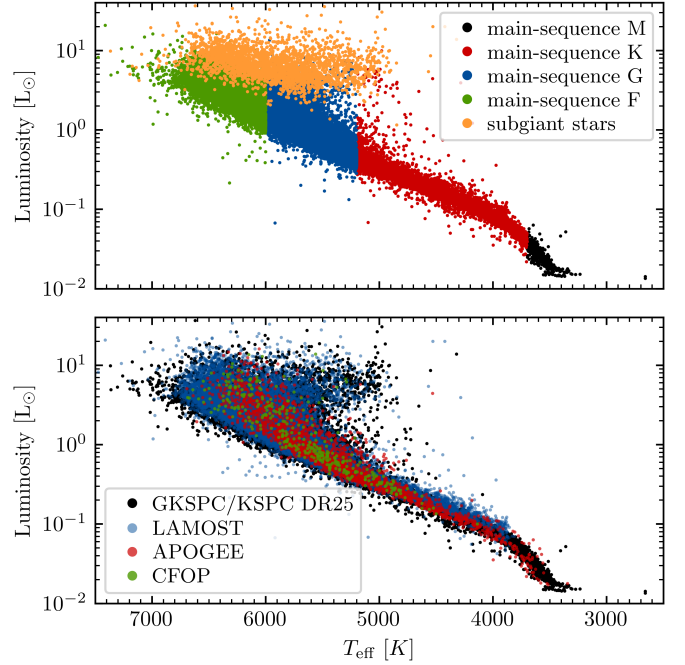
Fig. B.1. HR diagram for the target sample. The color code indicates to which subsample the targets belong to (top) and the source for the stellar properties (bottom).

Fig. B.2. $\sigma(S_{ph})$ as a function of the $\langle S_{ph}\rangle$. The black symbols show the target sample of the current study, while the red symbols show the targets that were removed according to a given criteria: *Kepler* magnitude, observational length, and potential binarity.

moved many outliers in particular with smaller $\sigma(S_{ph})$ or larger $\langle S_{ph}\rangle$ than expected.

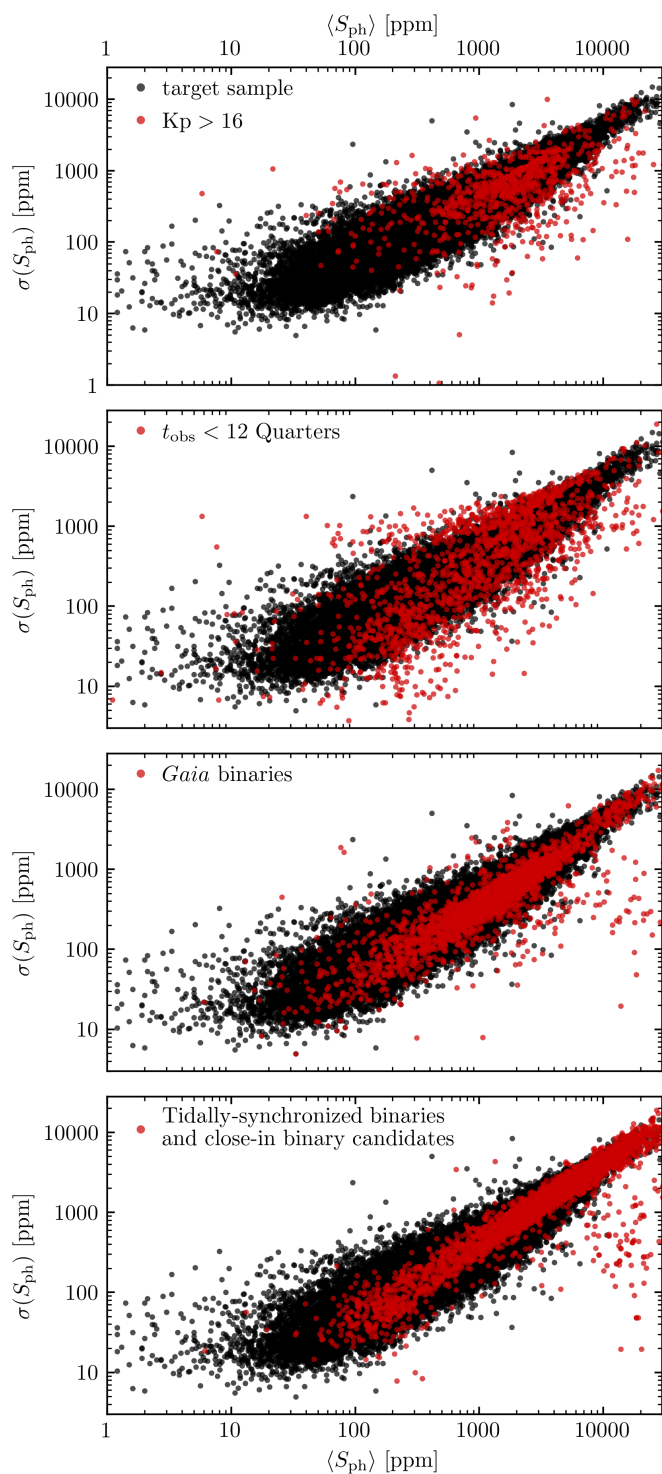While removing a large number of targets that follow the $\sigma(S_{ph})$ versus $\langle S_{ph}\rangle$ relation, it becomes clear that the majority of the outliers were eliminated by removing these potential contaminants. Thus, all the targets in red in Fig. B.2 were neglected from the analysis.

Finally, we also checked whether considering an additional selection criterion based on the RUWE from *Gaia* Early Data Release 3 (EDR3; Gaia Collaboration et al. 2016, 2021; Lindegren et al. 2021) changes the results. Targets with RUWE > 1.2 are often considered to be likely binaries. Our target sample has 6,464 targets with RUWE > 1.2, but we do not find that the targets with large RUWE are outliers in terms of S_{ph} and P_{rot} behavior. For this reason we decided to keep them in the target sample. In Table C.4, we summarize the results when neglecting these targets and show that the results and conclusions do not change significantly. Figure B.3 shows where those targets lie in the $\sigma(S_{ph})$ versus $\langle S_{ph}\rangle$ diagram.
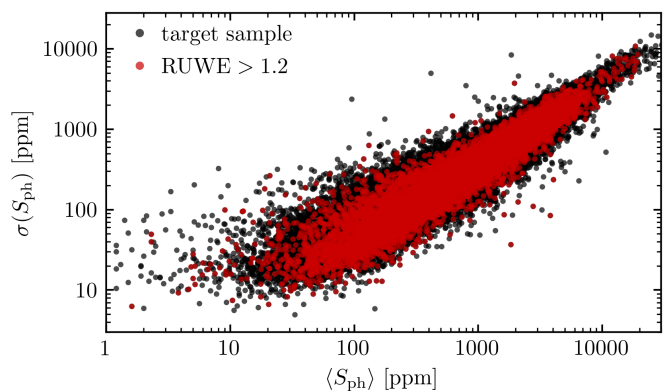
Fig. B.3. $\sigma(S_{ph})$ as a function of the $\langle S_{ph}\rangle$ for the target sample, where red highlights the targets with RUWE > 1.2.

Figure B.4 shows the rotation versus T_{eff} and activity versus T_{eff} diagrams color-coded by RUWE. The data points are ordered from the smallest (light red) to the largest (dark red) RUWE values, such that the latter overlap the former for better visualization of the targets with large RUWE. Most of the targets with large RUWE are within the normal parameters. There is a large concentration of dark data points in the location of the slow-rotating population, which could be expected because it is the most numerous population.

Appendix B.3: Bimodal rotation-period distribution: Slow- and fast-rotating populations

The distribution of rotation periods for *Kepler* targets is bimodal (e.g., McQuillan et al. 2014; Santos et al. 2019b, 2021a), particularly for the cool solar-like stars. The bimodality of P_{rot} leads to two populations or groups in the P_{rot} versus T_{eff} diagram with a region of low density in between (also called intermediate-P_{rot} gap). The discontinuity in the rotation distribution can also be seen in the activity-rotation diagrams, where two regimes seem to exist. While less pronounced for G dwarfs, S_{ph} depends on P_{rot} in both fast- and slow-rotating populations.

We used the discontinuity in the activity-rotation relation to split the GKM dwarfs into fast- and slow-rotating populations. While our samples, metrics, and approach differ from those in Reinhold & Hekker (2020), they also used these discontinuities

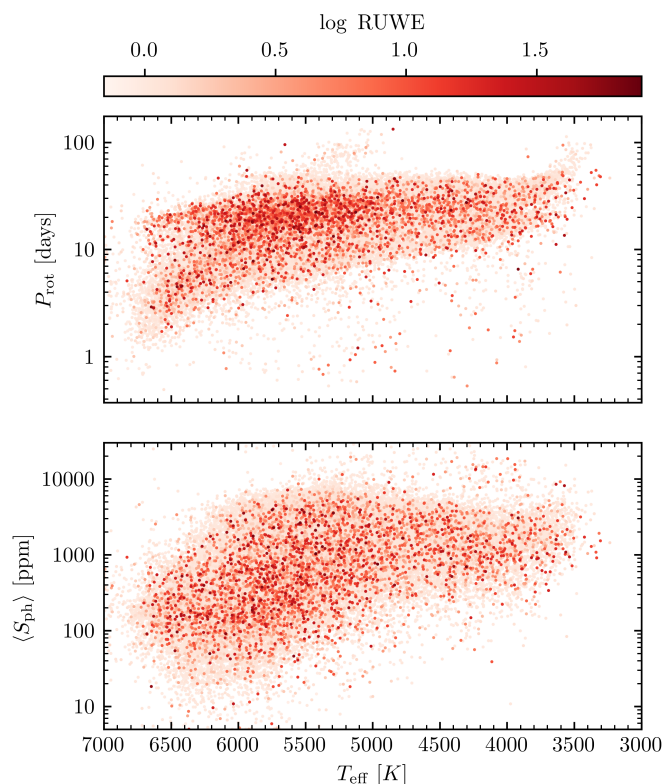**Fig. B.4.** $P_{\rm rot}$ (top) and $\langle S_{\rm ph} \rangle$ (bottom) as a function of the effective temperature for the stars in the target sample, including the subgiant stars. The color code indicates the RUWE values for each target.
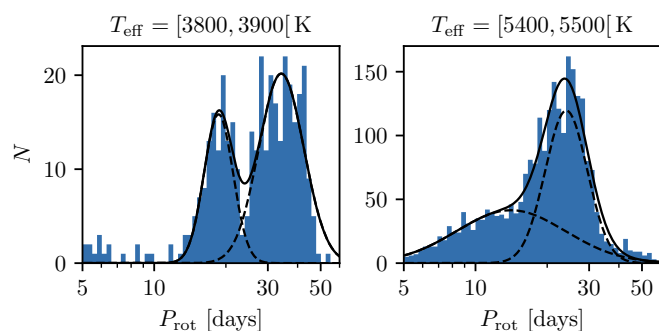

Fig. B.5. Rotation-period distribution for stars with $T_{\rm eff}$ within 3800 and 3900 K (left) and 5400 and 5500 K (right). The solid line shows the best fit with a double Gaussian, while the dashed lines show the individual Gaussian distributions.

to determine the location of the "gap" for solar-like stars observed during K2 (Howell et al. 2014).

First, we take $T_{\rm eff}$ intervals of 100 K from 3500 K to 6000 K (only a few stars are cooler than 3500 K). Figure B.5 shows two examples of the rotation-period distribution in such narrow intervals. While the bimodality of the $P_{\rm rot}$ distribution is clearer for the K and M dwarfs, the log $P_{\rm rot}$ distribution for G dwarfs is also well described by a double Gaussian.

For each $T_{\rm eff}$ interval, we determined the upper edge of the activity-rotation diagram by: 1) splitting the data now into log $P_{\rm rot}$ intervals of width 0.02 dex; and 2) computing the 95th percentile for the $\langle S_{\rm ph} \rangle$ in each interval (dotted red line in Fig. B.6). We then smoothed the upper edge with an uniform filter of size 3 (solid red) and determine the location of the local minimum between the two populations (black cross; through
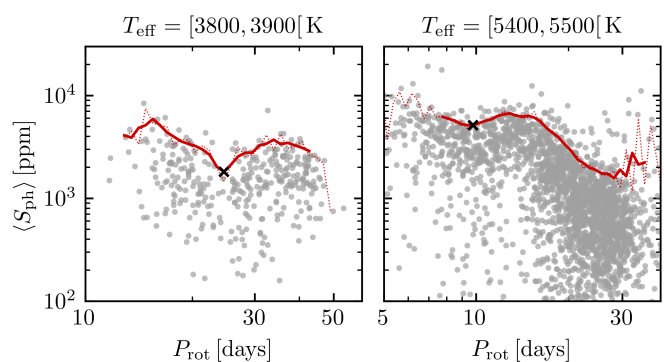

Fig. B.6. Activity-rotation diagram for two intervals of 100 K: 3800-3900 K (left); and 5400-5500 K (right). We use the local minimum (black crosses) to split the sample into fast- and slow-rotating populations. The gray dots show the stars with $T_{\rm eff}$ within the considered interval. The dotted red line shows the upper edge of the $\langle S_{\rm ph} \rangle$ distribution (95th percentile), while the solid red line shows its smoothed version.
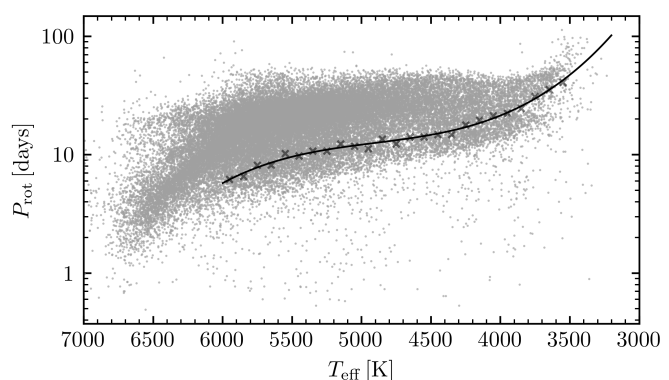
Fig. B.7. Rotation period as a function of the effective temperature for the main-sequence stars in our target sample. The black crosses show the position of the local minimum in the $\langle S_{\rm ph} \rangle$-$P_{\rm rot}$ diagram for each $T_{\rm eff}$ interval of 100 K (Fig. B.6). The black solid line shows the best fit with a third degree polynomial, which is adopted in this work to split the slow- and fast-rotating populations.

bounded minimization). For the minimization procedure, we neglected the regions with few stars, where the upper edge is not well defined. Figure B.6 shows two examples, for the same $T_{\rm eff}$ intervals as in Fig. B.5.

Figure B.7 shows the rotation period as a function of $T_{\rm eff}$ for the main-sequence stars in our sample. The crosses mark the local minima found in the previous step (Fig. B.6) and the solid line corresponds to the best fit to the local minima with a third degree polynomial. We adopted this polynomial as the transition between the two regimes for GKM dwarfs.

Appendix B.4: Sun- and Doris-like stars

In Sect. 4.3, we select stars with very similar properties ($T_{\rm eff}$, L, and $P_{\rm rot}$) to those of the Sun (i.e., Sun-like stars). Since the work by Reinhold et al. (2020), the stellar properties have been updated (Ahumada et al. 2020; Zong et al. 2020; Berger et al. 2020; Santos et al. 2021a). In this subsection we provide more details on the Sun-like stars in our sample and their previous classification. We also compare the properties of the Sun- and Doris-like stars in comparison with the G dwarf sample.

The Sun-like sample is composed of 211 stars (Sect. 4.3). These are stars within 100 K around $T_{\rm eff\odot}$, 0.3 around $L_\odot$, and

2 days around $P_{rot\odot}$. In terms of rotation-period estimates, from the 211 stars, 43 are in the periodic sample of McQuillan et al. (2014) and 158 in their nonperiodic sample. 10 stars were not part of their analysis. Figure B.8 compares the current T_{eff} and log g^7 values with those available previously from KSPC DR25 (simply DR25 in Fig. B.8). Many of the targets classified in this work as Sun-like had KSPC DR25 properties inconsistent with Sun-like. In KSPC DR25, most targets were considered to be hotter than current constraints. The average difference between the previous and current T_{eff} values is 129.1 K, while the for log g is 0.01 dex.
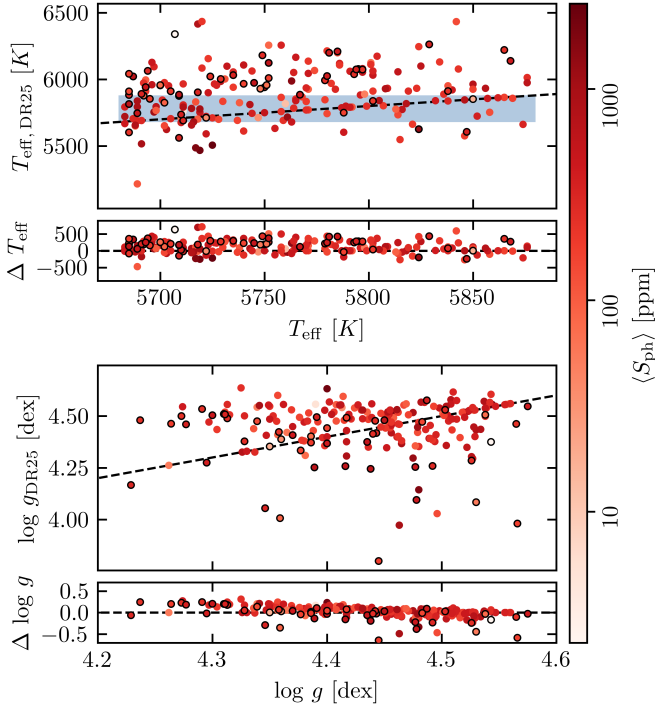

Fig. B.8. Comparison between the current values for T_{eff} and log g (x-axis) and those from KSPC DR25 (y-axis) for the Sun-like sample. ΔT_{eff} and Δ log g correspond to the difference between previous and current constraints. The data points are colored according to their $\langle S_{ph} \rangle$. The dashed lines mark the 1-1 lines and the zero difference. The blue shaded region marks the T_{eff} interval we consider in this study to select Sun-like stars.

As noted in Sects. 4.4 and 4.5 the Doris-like stars are more metallic than what would be expected for the *Kepler* field. Figure B.9 shows the [Fe/H] distributions for the full G-dwarf sample (shaded gray), the Sun-like stars (dashed red), and the Doris-like stars (dotted red). The median values are indicated in the top figures. For the Sun-like sample, there is an excess of stars with solar metallicity in comparison with the distribution for the full G-dwarf sample. For the Doris-like sample, within that T_{eff} and L range and with such P_{rot}, there is a large number of high metallicity stars.

Figure B.10 shows the distributions of P_{rot} and the relative uncertainty for Sun- (left) and Doris-like (right) samples in comparison with the distribution for the G dwarfs with similar P_{rot} (shaded gray; full T_{eff} range, i.e., within 5200 and 6000 K). The P_{rot} distributions show a similar behavior, with a higher fraction of detections for shorter P_{rot} than for longer P_{rot} in this parameter

space. Therefore, the bias toward shorter P_{rot} is expected in the Sun- and Doris-like samples. The P_{rot} uncertainty is in average $\sim$ 10%, which is consistent with the values for the full *Kepler* sample (Santos et al. 2021a).
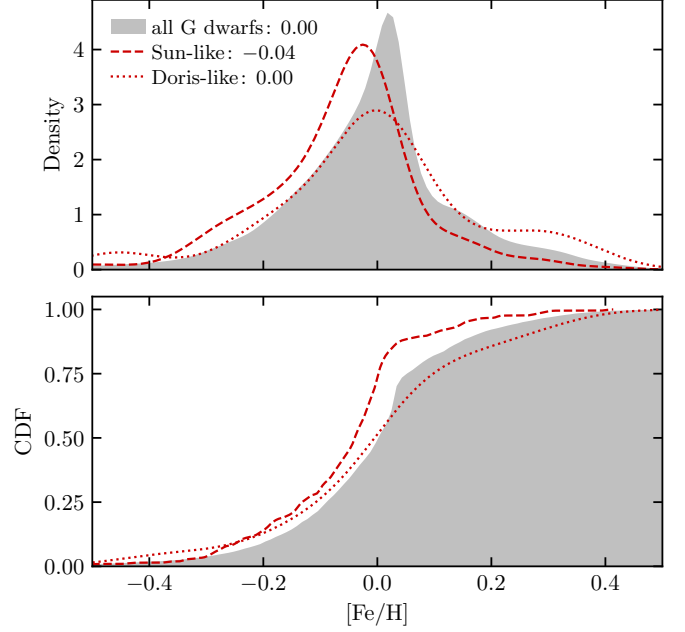
Fig. B.9. [Fe/H] distribution for the full G-dwarf sample (shaded gray), the Sun-like stars (dashed red), and the Doris-like stars (dotted red). The bottom panel shows the CDFs, where one can identify more clearly the differences between the samples. The median values of the distributions are also identified.
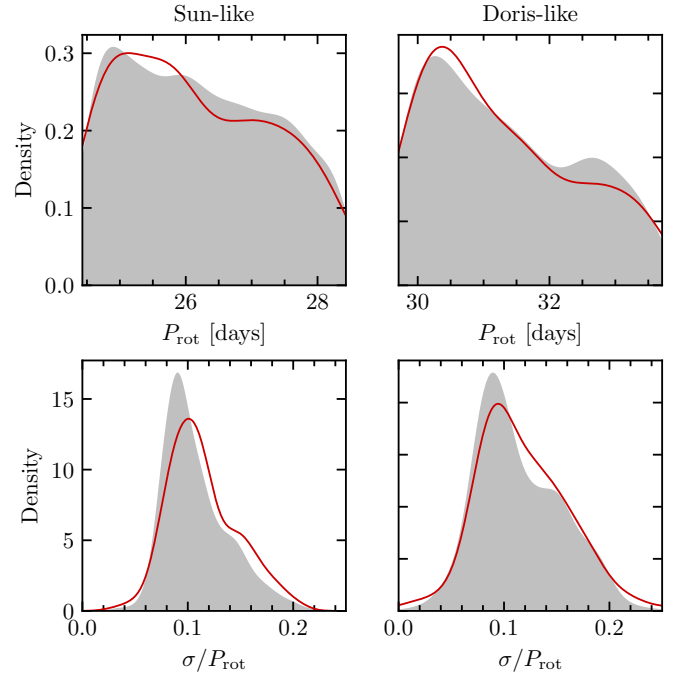
Fig. B.10. Comparison between the distributions of P_{rot} (top) and relative uncertainty (bottom) for the G dwarfs with P_{rot} within $P_{rot\odot} \pm 2$ (shaded gray) and the Sun-like (left) and Doris-like (right) samples (red).

---

[7] We opted to use luminosity instead of log g in our analysis. Nevertheless, the final results are consistent whether we adopt L or log g.
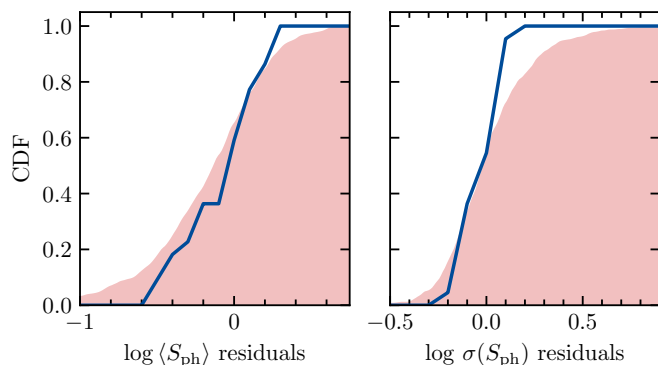
Fig. B.11. Same as in Fig. 8 but when considering the period estimate from the GWPS.

Fig. C.1. Difference between SCCs and PCCs for all the relations considered in the tables above.

As seen in Appendix A, there is some discrepancy between the period estimates from the rotational analysis of VIRGO g+r. The estimates agree within the error bars, but the $P_{\rm GWPS} = 22.87$ d underestimates $P_{\rm rot\odot}$. Similarly to Fig. 8, Fig. B.11 compares the CDF of the $\langle S_{\rm ph} \rangle$ and $\sigma(S_{\rm ph})$ residuals for the Sun and the stars with similar $T_{\rm eff}$ and L to the Sun and $P_{\rm rot}$ within $P_{\rm GWPS} \pm 2$ d. This selection adds more low-activity stars in comparison to the Sun-like stars but the distributions are comparable.

Appendix C: Multivariate linear regression

To account for possible dependences on different stellar properties and isolate each dependence, we perform multivariate linear regressions. In the main text we summarize the main results and in this section we provide the regression coefficients and parameters for other subsets of the main sample.

Tables C.1- C.5 show the regression coefficients related to Tables 1, 2, and 3. Table C.4 lists the correlation coefficients and the multivariate regression coefficients when neglecting targets with RUWE>1.2 (Sect. B.2). The results and conclusions do not change significantly. The same is found when considering solely the targets with spectroscopic atmospheric parameters (Table C.5). For M dwarfs, the results change significantly, with moderate correlations found between the $S_{\rm ph}$ variation and $T_{\rm eff}$, L, and [Fe/H]. However, the number of available targets is very small and may be the cause for such results.

Finally, we adopt the SCC as it does not assume a specific function form for the relationships between the different parameters. Nevertheless, we also have computed the Pearson correlation coefficients (PCCs), which assume linear relations. Figure C.1 shows the distribution of the difference between the SCCs and PCCs corresponding to the cases in all the above tables (total of 183 relations). The distribution is centered in zero and is consistent with small differences between SCCs and PCCs, which indicates that the assumption made by the multivariate regression is still valid.

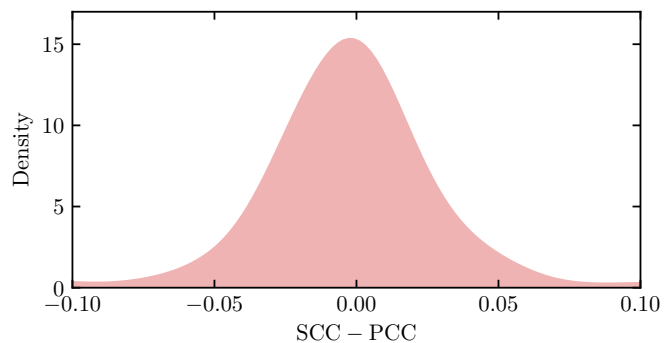|	main sequence				subgiant
	M	K	G	F	
c_0	-0.61	0.16	0.68	1.24	0.97
$c_{\rm Kp}$	1.0×10^{-2}	1.3×10^{-2}	2.7×10^{-2}	5.2×10^{-2}	4.4×10^{-2}
$c_{t_{\rm obs}}$	-5.6×10^{-3}	-1.5×10^{-2}	-2.4×10^{-2}	-5.2×10^{-2}	-4.3×10^{-2}
$c_{T_{\rm eff}}$	1.8×10^{-4}	3.4×10^{-5}	-4.1×10^{-5}	-1.1×10^{-4}	-1.1×10^{-4}
c_L	1.7×10^{0}	-6.5×10^{-3}	-2.0×10^{-2}	-1.4×10^{-2}	8.8×10^{-4}
$c_{\rm [Fe/H]}$	4.3×10^{-2}	3.0×10^{-2}	1.6×10^{-2}	-8.1×10^{-2}	-3.9×10^{-2}
$c_{P_{\rm rot}}$	-4.9×10^{-3}	-6.2×10^{-3}	-8.4×10^{-3}	-4.6×10^{-3}	-2.4×10^{-3}
$c_{\log \langle S_{\rm ph}\rangle}$	8.8×10^{-1}	8.2×10^{-1}	7.8×10^{-1}	7.2×10^{-1}	7.8×10^{-1}

FAST-ROTATING POPULATION

	M	K	G
c_0	0.12	0.38	0.84
$c_{\rm Kp}$	3.9×10^{-3}	1.1×10^{-2}	7.0×10^{-3}
$c_{t_{\rm obs}}$	-1.4×10^{-2}	-1.8×10^{-2}	-2.5×10^{-2}
$c_{T_{\rm eff}}$	1.4×10^{-4}	-1.2×10^{-5}	-3.0×10^{-5}
c_L	-1.7×10^{0}	-2.2×10^{-3}	-7.1×10^{-3}
$c_{\rm [Fe/H]}$	4.2×10^{-2}	3.2×10^{-2}	3.0×10^{-2}
$c_{P_{\rm rot}}$	-6.5×10^{-3}	-1.1×10^{-2}	-1.4×10^{-2}
$c_{\log \langle S_{\rm ph}\rangle}$	8.2×10^{-1}	8.5×10^{-1}	8.1×10^{-1}

SLOW-ROTATING POPULATION

	M	K	G
c_0	-2.86	0.23	0.65
$c_{\rm Kp}$	2.1×10^{-2}	1.3×10^{-2}	2.9×10^{-2}
$c_{t_{\rm obs}}$	1.4×10^{-3}	-1.4×10^{-2}	-2.4×10^{-2}
$c_{T_{\rm eff}}$	6.7×10^{-4}	2.7×10^{-5}	-3.7×10^{-5}
c_L	5.2×10^{0}	-6.2×10^{-3}	-2.7×10^{-2}
$c_{\rm [Fe/H]}$	1.7×10^{-1}	3.2×10^{-2}	2.1×10^{-2}
$c_{P_{\rm rot}}$	-4.4×10^{-3}	-6.9×10^{-3}	-8.4×10^{-3}
$c_{\log \langle S_{\rm ph}\rangle}$	9.6×10^{-1}	8.1×10^{-1}	7.7×10^{-1}

Table C.1. Coefficients from the multivariate regression summarized in Table 1, where c_0 is the constant term.

$\langle S_{\rm ph}\rangle$		
	$T_{\rm eff\odot} \pm 100$ K $L_\odot \pm 0.3$	$T_{\rm eff,\ Doris} \pm 100$ K $L_{\rm Doris} \pm 0.3$
c_0	3.98	4.18
$c_{T_{\rm eff}}$	3.0×10^{-4}	1.8×10^{-4}
c_L	-9.7×10^{-1}	-1.0×10^{0}
$c_{\rm [Fe/H]}$	6.6×10^{-1}	5.5×10^{-1}
$c_{\log P_{\rm rot}}$	-1.6×10^{0}	-1.2×10^{0}

$\sigma(S_{\rm ph})$		
c_0	1.27	0.67
$c_{T_{\rm eff}}$	-1.1×10^{-4}	-3.3×10^{-5}
c_L	-1.2×10^{-1}	-6.6×10^{-2}
$c_{\rm [Fe/H]}$	4.0×10^{-3}	1.8×10^{-2}
$c_{P_{\rm rot}}$	-9.8×10^{-3}	-8.8×10^{-3}
$c_{\log S_{\rm ph}}$	7.6×10^{-1}	7.8×10^{-1}

Table C.2. Regression coefficients for all Sun- and Doris-like stars (concerning Tables 2 and 3).

$\langle S_{\rm ph}\rangle$		
	$T_{\rm eff\odot} \pm 100$ K $\log g_\odot \pm 0.1$ dex	$T_{\rm eff,\ Doris} \pm 100$ K $\log g_{\rm Doris} \pm 0.1$ dex
c_0	6.77	4.01
$c_{T_{\rm eff}}$	-1.5×10^{-4}	2.3×10^{-4}
c_L	-6.7×10^{-1}	-9.0×10^{-1}
$c_{\rm [Fe/H]}$	$9/0 \times 10^{-1}$	7.0×10^{-1}
$c_{\log P_{\rm rot}}$	-2.1×10^{0}	-1.4×10^{0}

$\sigma(S_{\rm ph})$		
c_0	1.43	0.49
$c_{T_{\rm eff}}$	-1.5×10^{-4}	-1.9×10^{-5}
c_L	-1.4×10^{-1}	-9.4×10^{-2}
$c_{\rm [Fe/H]}$	6.8×10^{-2}	3.8×10^{-2}
$c_{P_{\rm rot}}$	-9.9×10^{-3}	-7.3×10^{-3}
$c_{\log \langle S_{\rm ph}\rangle}$	7.8×10^{-1}	8.1×10^{-1}

Table C.3. Same as in Table C.2 but only for the stars with spectroscopic constraints.

		main sequence				
		M	K	G	F	subgiant
	N stars	308	10,850	16,306	6,117	2,117
	$\langle S_{ph} \rangle_{5th}$	630.37	287.1	83.6	29.3	37.7
	$\langle S_{ph} \rangle_{95th}$	5776.2	5211.4	4994.5	2118.3	4624.4
SCC	Kp	0.03	0.07	0.14	0.30	0.19
	t_{obs}	0.01	-0.10	-0.12	-0.20	-0.18
	T_{eff}	0.12	0.10	-0.07	-0.16	-0.23
	L	-0.12	0.00	-0.10	-0.16	0.05
	[Fe/H]	-0.04	0.05	0.00	-0.01	-0.02
	P_{rot}	-0.33	-0.36	-0.37	-0.17	-0.16
	$\langle S_{ph} \rangle$	0.82	0.91	0.94	0.88	0.88
	c_0	-1.39	0.16	0.73	1.34	1.06
	c_{Kp}	4.2×10^{-3}	1.3×10^{-2}	2.5×10^{-2}	5.5×10^{-2}	4.1×10^{-2}
	$c_{t_{obs}}$	-3.6×10^{-3}	-1.6×10^{-2}	-2.4×10^{-2}	-4.8×10^{-2}	-4.5×10^{-2}
	$c_{T_{eff}}$	3.8×10^{-4}	3.6×10^{-5}	-4.4×10^{-5}	-1.4×10^{-4}	-1.2×10^{-4}
	c_L	-2.0×10^0	-9.4×10^{-3}	-1.9×10^{-2}	-1.6×10^{-2}	1.4×10^{-3}
	$c_{[Fe/H]}$	-3.1×10^{-2}	3.7×10^{-2}	4.9×10^{-3}	-8.8×10^{-2}	-3.3×10^{-2}
	$c_{P_{rot}}$	-4.3×10^{-3}	-6.2×10^{-3}	-8.4×10^{-3}	-5.3×10^{-3}	-2.2×10^{-3}
	$c_{\log \langle S_{ph} \rangle}$	9.1×10^{-1}	8.2×10^{-1}	7.7×10^{-1}	7.1×10^{-1}	7.8×10^{-1}

Table C.4. Same as in Tables 1 and C.1, but when neglecting targets with RUWE>1.2.

		main sequence				
		M	K	G	F	subgiant
	N stars	31	2,946	7,767	4,507	1,629
	$\langle S_{ph} \rangle_{5th}$	902.9	266.1	63.6	28.1	33.1
	$\langle S_{ph} \rangle_{95th}$	8504.9	5346.3	4880.7	1571.7	3247.0
SCC	Kp	-0.02	0.00	0.04	0.18	0.10
	t_{obs}	0.02	-0.11	-0.14	-0.20	-0.15
	T_{eff}	0.24	0.06	-0.10	-0.15	-0.26
	L	-0.33	0.00	-0.16	-0.19	0.04
	[Fe/H]	0.10	0.02	0.02	-0.06	-0.05
	P_{rot}	-0.43	-0.37	-0.36	-0.13	-0.11
	$\langle S_{ph} \rangle$	0.85	0.92	0.95	0.88	0.87
	c_0	-0.86	0.51	1.23	1.75	1.48
	c_{Kp}	-5.2×10^{-2}	1.4×10^{-3}	1.0×10^{-2}	4.9×10^{-2}	3.1×10^{-2}
	$c_{t_{obs}}$	1.1×10^{-2}	-3.1×10^{-2}	-4.3×10^{-2}	-6.9×10^{-2}	-5.7×10^{-2}
	$c_{T_{eff}}$	4.2×10^{-4}	2.3×10^{-5}	-6.0×10^{-5}	-1.2×10^{-4}	-1.4×10^{-4}
	c_L	-3.7×10^0	-4.0×10^{-3}	-2.8×10^{-2}	-1.6×10^{-2}	3.2×10^{-4}
	$c_{[Fe/H]}$	1.9×10^{-1}	4.1×10^{-2}	1.2×10^{-2}	-7.9×10^{-2}	-5.7×10^{-2}
	$c_{P_{rot}}$	-4.7×10^{-3}	-6.0×10^{-3}	-7.8×10^{-3}	-4.2×10^{-3}	-1.7×10^{-3}
	$c_{\log \langle S_{ph} \rangle}$	9.1×10^{-1}	8.5×10^{-1}	8.1×10^{-1}	7.2×10^{-1}	7.8×10^{-1}

Table C.5. Same as in Tables 1 and C.1, but when considering only the targets with spectroscopic atmospheric parameters.